Electromagnetic ion cyclotron waves at proton cyclotron harmonics

C. C. Chaston, J. W. Bonnell, J. P. McFadden, R. E. Ergun, and C. W. Carlson

Space Sciences Laboratory, University of California, Berkeley, California, USA

[1] Waves with frequencies in the vicinity of the proton cyclotron frequency and its harmonics are commonly observed from the Fast Auroral Snapshot spacecraft when traversing regions of auroral particle acceleration. In areas of upward current, large-amplitude electromagnetic waves with frequencies within 5% of the local proton gyrofrequency Ω_p and its harmonics are often observed where upstreaming ion beams exist. These waves have electric field (E_1) and magnetic field (B_1) amplitudes of up to 1 V m^{-1} and 2 nT with the ratio E_1/B_1 as small as c. The waves occur in the low-altitude portion of the primary auroral acceleration potential, where plasma densities are ≤ 1 cm^{-3}. It is shown how these waves grow through inverse Landau resonance with a cold field-aligned electron beam superimposed on an accelerated and magnetically mirrored plasma sheet electron component in the absence of any significant plasma densities at energies below ~ 100 eV. Significantly, the drift velocity of the cold beam (v_{oeb}) is several times larger than its thermal velocity v_{eb}, and it is this feature that allows the wave to become electromagnetic at cyclotron harmonics while simultaneously giving rise to broadband electrostatic emissions spanning the first few cyclotron harmonics as is observed. INDEX TERMS: 2704 Magnetospheric Physics: Auroral phenomena (2407); 2772 Magnetospheric Physics: Plasma waves and instabilities; 6984 Radio Science: Waves in plasma; 7871 Space Plasma Physics: Waves and instabilities

1. Introduction

[2] The importance of ion cyclotron waves in auroral physics lies in their ability to heat ions, accelerate/modulate electrons, and perhaps to provide anomalous resistivity, allowing the creation of a parallel potential drop. Since such processes have global implications for the magnetosphere, these waves have been the subject of numerous publications [*Bergmann*, 1984; *Temerin and Lysak*, 1984; *Andre*, 1985a; *Cattell et al.*, 1991, 1998; *Koskinen*, 1997; *Oscarsson et al.*, 1997; *McFadden et al.*, 1998a; *Erlandson and Zanetti*, 1998]. The topic of this report concerns ion cyclotron waves around the proton cyclotron frequency Ω_p and its harmonics in the upward current regions of the auroral oval. Similar waves at frequencies close to the harmonics of the proton cyclotron frequency have been identified in the equatorial magnetosphere [*Perraut et al.*, 1982], planetary foreshocks [*Smith et al.*, 1985], and comets [*Glassmeier et al.*, 1989]. However, the waves studied in this report are most closely related to what has previously been called electrostatic ion cyclotron waves identified in ion beam regions at altitudes of greater than 1 R_E above the auroral oval from the Viking, ISEE 1, and S3-3 spacecraft [*Andre et al.*, 1986; *Cattell et al.*, 1991; *Kintner et al.*, 1979] with frequencies of the order of 1.2 Ω_p.

[3] Observations from the Fast Auroral Snapshot (FAST) spacecraft at ~ 4000 km altitude in ion beam regions [*Cattell et al.*, 1998; *Chaston et al.*, 1998; *Ergun et al.*, 1998a; *McFadden et al.*, 1998a] show waves at $n\Omega_p$ that are electromagnetic. *Chaston et al.* [1998] has shown that these waves can have Poynting fluxes directed upward out of the auroral oval, suggesting that the waves observed at higher altitudes may have their source at the base of the auroral potential structure where they are electromagnetic. As these waves travel up the fieldline, the normalized wave frequency ω/Ω_p increases owing to the weakening geomagnetic field, and the waves become increasingly electrostatic as they refract across the "electrostatic ion cyclotron wave" dispersion surfaces in the direction of increasing $k_\parallel$. This does not mean that the waves observed at higher altitudes cannot be driven locally, but rather it suggests another possible source.

[4] These waves grow from free energy sources made available owing to the acceleration of the electron and ions populating the upward current regions of the auroral oval. Primarily, these plasmas are of magnetospheric and ionospheric origin with solar wind or magnetosheath plasmas contributing only a small fraction except when in the cusp. Recent observations [*McFadden et al.*, 1999] have shown that in upward current regions where ion beams exist there is a depletion or absence of an unaccelerated ionospheric component. This is consistent with the electrostatic model of the aurora [*Mozer et al.*, 1977], where a parallel electric

field exists thereby making the presence of any unaccelerated component with temperature less than the magnitude of the parallel potential drop problematic. Since the field-aligned auroral potential drop is of the order of kilovolts and plasma sheet and ionospheric electron temperatures are less than 1 keV and 10 eV, respectively, it can be expected that electron distributions present in these regions will consist of accelerated magnetospheric and ionospheric electrons.

[5] The magnitude of the auroral potential drop relative to the temperature of the components of the plasma is a crucial measurement in determining which wave modes will be excited. When the beam velocity of the electron component (v_{oe}) exceeds its thermal velocity v_{eb}, wave growth becomes so rapid that cyclotron motion is disrupted to such an extent that the ions in the plasma become demagnetized, thereby removing any structuring around this frequency and leading to broadband wave growth. Previously, it has been expected that such a condition is unlikely to occur owing to the rapid heating of the electron component as its drift speed approaches its thermal speed.

[6] For ionospheric electrons the required potentials, necessary for $v_{oe}/v_{eb} > 1$ in the absence of heating, are small and certainly much smaller than typical auroral potentials. For the low total density, observations at altitudes of 4000 km current continuity and the conservation of magnetic flux indicate that large portions of the auroral potential may be concentrated over distances along the fieldline of the order of a hundred kilometers requiring parallel electric fields in excess of 10 mV m^{-1} [*Ergun et al.*, 2000]. Such fields may provide $v_{oe}/v_{eb} > 1$.

[7] The results reported here show that given an ionospheric source population of electrons it is possible (in the continuously driven case) to accelerate these electrons to velocities exceeding their thermal speed before the distribution is thermalized in the parallel direction. Here we show this to be true from direct particle measurements and indirectly from the properties of the observed ion wave emissions. The driver in this case is, of course, the parallel electric field, which continuously replenishes the distribution at a given altitude with newly accelerated plasma sheet electrons from above and ionospheric electrons that may **E** × **B** drift or diffuse into the accelerating potential drop from the sides [*Lotko*, 1986]. This scenario is particularly relevant at the base of the auroral acceleration potential since it is here where the parallel field is thought to be strongest and where FAST observes wave emissions, requiring the electron drift velocity to exceed the parallel electron thermal speed.

[8] This paper is organized in sections devoted to describing wave and particle observations (section 2), wave dispersion analysis (section 3), and the effects on wave dispersion of large parallel electron drift speeds (section 4) and cold plasma density (section 5). In section 6 we place the theoretical results obtained in context with wave modeling performed previously by other researchers and simulate the intense ion heating observed in conjunction with these waves. Section 7 then summarizes the findings of this study.

2. Observations
2.1. Overview

[9] Figure 1a presents a summary of the plasma environment typical of regions where electromagnetic waves at cyclotron harmonics are observed. This is the same interval shown by *Elphic et al.* [1998]. Figure 1a shows features classically associated with the electrostatic shocks first reported by *Mozer et al.* [1977] and recently reiterated with observations from FAST as reported by *Carlson et al.* [1998] and *Ergun et al.* [1998a]. At this time, FAST is at apogee with an altitude of ∼4100 km over the premidnight oval. Magnetically conjugate aircraft-borne all-sky camera observations show that at this time, FAST is passing through an auroral spiral [*Stenbaek-Nielsen et al.*, 1998]. The spacecraft remains above the accelerating potential in both the downward and upward current regions except when in transition from one current direction to another or presumably when in the center of the spiral at 0926:47 UT. Of specific interest to this report is the wave activity shown in the time series and spectral result of Figures 1a and 1b extending from 0926:11 to 0927:08 UT. These waves have amplitudes of up to 1 V m^{-1} in $E_{1\perp}$ (E_{S-N}) and 2 nT in $B_{1\perp}$ (B$_{E-W}$). The spectral results (Figure 1b) over this interval show a set of discrete narrowband harmonics centered on multiples of the proton cyclotron frequency Ω_p superimposed on a background of broadband turbulence.

[10] The electron spectra (Figure 1c) at this time shows a sharp mono-energetic peak with a depletion of flux below a few hundred eV, consistent with the spacecraft traversing above a portion of the field-aligned potential drop. From a consideration of plasma quasi-neutrality it has been shown that the presence of counts at energies below 100 eV in such regions is due to photoelectrons [*McFadden et al.*, 1999]. The depletion of the cold electron population in the accelerating potential will later be shown to be essential to explaining the observed wave properties. Note how fluxes at the peak energies during the time of the most intense harmonic emissions are modulated. Also at this time the pitch angle spectra (Figure 1d) show that the electron distribution becomes strongly field-aligned (0°/360° being downward in the north) with enhanced downgoing fluxes over a width similar to that of the loss cone. The presence of a cool field-aligned beam is an another ingredient essential to accurately modeling the observed emissions.

[11] The ion energy spectra is in appearance similar to that of the electrons. The integrated electric field shown by the black trace in Figure 1e indicates that the energy of the ion beam is at most times consistent with acceleration through a potential drop static over at least an ion transit time. Not surprisingly, the waves at the proton cyclotron harmonics significantly disturb the upstreaming ion distribution, scattering the ions to pitch angles approaching 90°/270° (Figure 1f). This is a common feature seen in conjunction with such waves and is a particularly ion-mass-selective heating process. Since the mass spectrometer instrument on FAST (TEAMS) supplies one gyrotropic distribution per half spin, the times series of the energy spectra as the spacecraft rotates reveals some pitch angle information. Figure 1i shows the pitch angle as a function of time for the instrument and when compared to the mass specific data of the He$^+$ and O$^+$ spectra (Figures 1g and 1h) shows enhanced fluxes once per spin at 180°. This is the ion beam. The width of these enhancements along the x axis (which is time or pitch angle) indicates the angular width of the beam. At the time when the protons show the most scattering in pitch angle (indicated by Figure 1f), the heavier
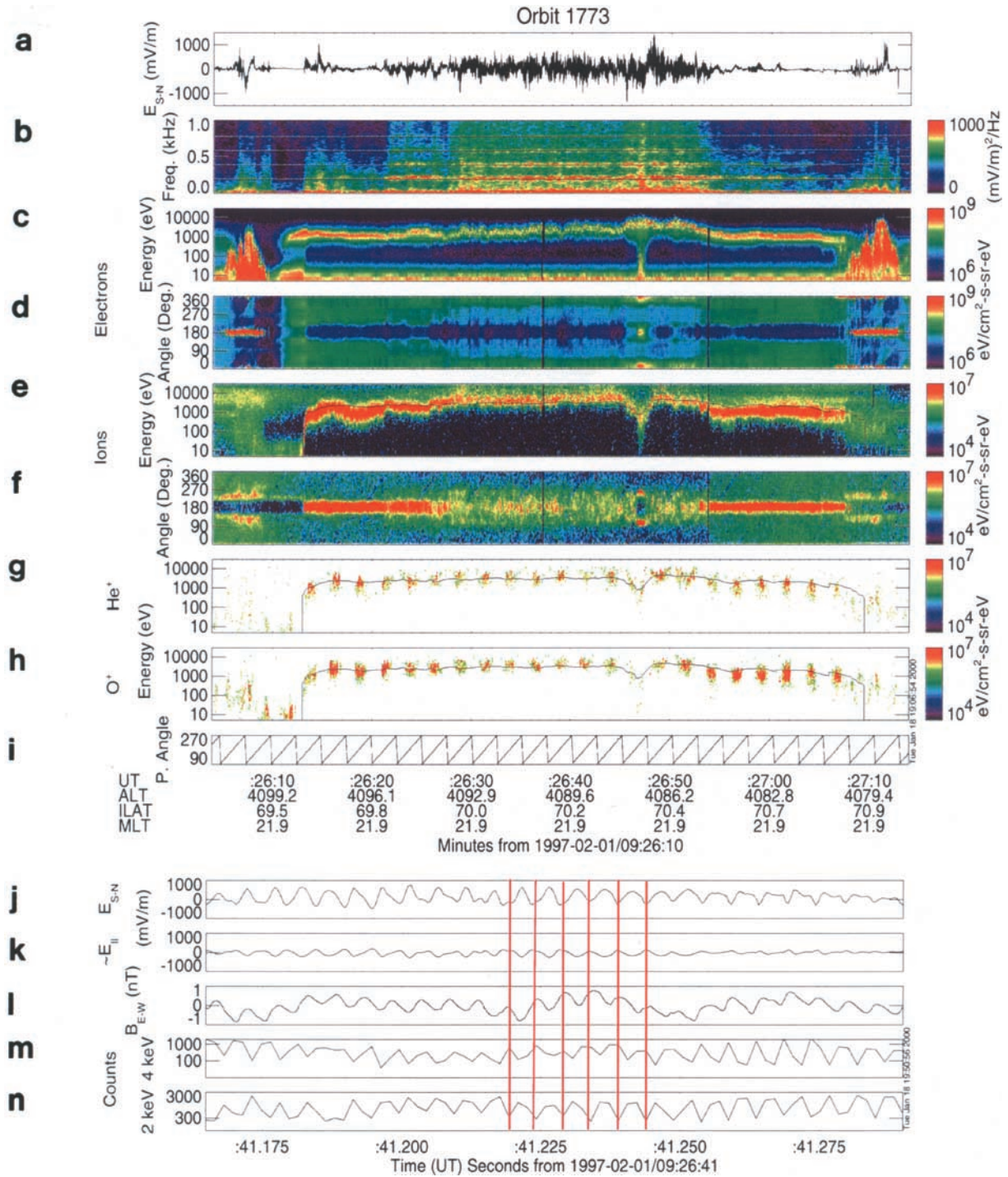
Figure 1. At the top summary plot for a FAST traversal through the premidnight auroral oval: (a) the DC electric field measured along the spacecraft trajectory (approximately south-north), (b) the electric field wave spectrum up to 10 kHz, where the horizontal lines indicate multiples of the proton cyclotron frequency Ω_p, (c, d) the electron energy and pitch angle spectra in units of differential energy flux, (e, f) the ion energy and pitch angle spectra in units of differential energy flux, (g, h) the He^+ and O^+ energy spectra, and (i) the look direction in pitch angle of the mass spectrometer instrument. The black trace superimposed on the energy spectra is the integrated electric field along the spacecraft trajectory. The vertical black lines in Figures 1c–1f represent a data gap. At the bottom, snapshots of the electric and magnetic field waveforms and fixed energy electrostatic analyzer data: (j) the electric field measured along the spacecraft trajectory, (k) the electric field measured close to B_0 (within 5°), (l) the magnetic field measured transverse to the spacecraft trajectory (approximately east-west) and perpendicular to B_0, (m, n) measurements made by the electrostatic analyzer experiment at fixed energies (sesa) of 4 and 2 keV, respectively.
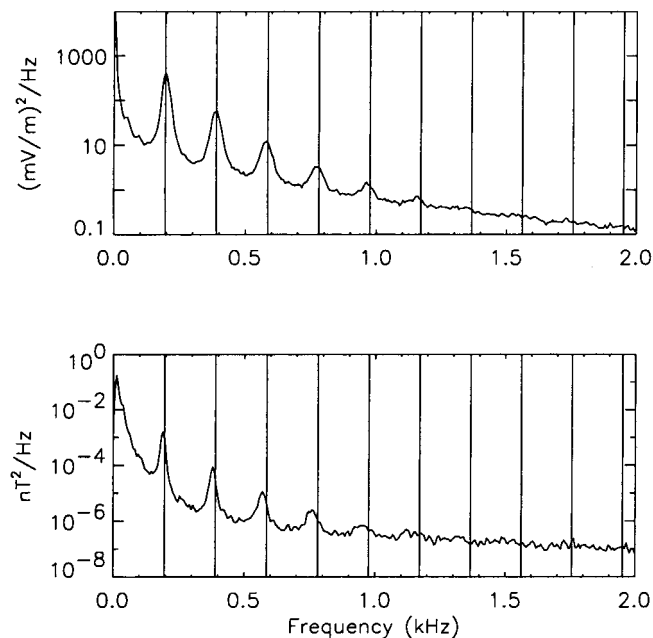
Figure 2. Average electric and magnetic field spectra over the interval from 0926:25 to 0926:55 UT shown in Figure 1. The vertical lines are multiples of the averaged proton cyclotron frequency Ω_p for the same interval.

ions show no real increased angular width, and in the case of oxygen the angular width appears to get narrower. The heavy ion spectra shown in these panels also match the potential inferred from the integrated perpendicular electric field consistent with electrostatic acceleration along the field line.

2.2. Wave Properties

[12] Figures 1j–1n show an example of the observed waveform in the electric and magnetic fields and the observed modulation in electron count rates. The electric field waveform while periodic at Ω_p is often not sinusoidal but is rather of a sawtooth form similar to that expected of non-linearity in electrostatic ion cyclotron waves as modeled by *Temerin et al.* [1979]. These features generally become more pronounced at larger amplitudes and in the presence of very energetic and cool electron beams. In the parallel component we see that waves may develop a significant bipolar parallel component of a spiky form as shown by *Ergun et al.* [1998a] with amplitudes in some cases that may be equal to that of the transverse wave field. At times the spikes are similar in form to the ion acoustic solitary waves with an e field polarity consistent with the passage of an ion phase space hole traveling up the field line with the ion beam. The magnetic field fluctuation in this case has an amplitude of $\sim$0.5 nT, yielding roughly $(E_1/B_1)/c\sim3$. The red lines superimposed on Figure 1l show that the parallel wave field is positively correlated with counts in the 4 keV electron channel and anticorrelated with counts in the 2 keV channel. These two energies straddle the characteristic energy of the mono-energetic peak found in the electron spectra shown in Figure 1c. The out of phase oscillations in the counts at 2 and 4 keV and the correlation with the parallel field indicate a direct modulation of the energy of the

electron mono-energetic peak in the parallel ion cyclotron wave field (where a positive value is an upward field) of the order of a keV as reported earlier by *McFadden et al.* [1998a]. It is later shown in the discussion of the dispersion results how such a modulation arises naturally in the parallel electric field of the ion cyclotron wave.

[13] Figure 2 shows the electric and magnetic field spectra averaged over the interval where harmonic waves are observed. The electric field spectrum, shown in the top panel, shows up to six harmonics very closely centered on $n\Omega_p$. Each successive harmonic occurs with progressively lower spectral energy density. In the magnetic field spectra a similar pattern exists; however, each peak is narrower and occurs at frequencies slightly below $n\Omega_p$. The magnitude of the frequency shift of the peak below each harmonic of Ω_p is $n\Delta\omega$, where $\Delta\omega$ is the frequency difference at Ω_p. In this way the frequency difference between each peak in the spectra for both the electric and magnetic field remains the same for all n. It is shown in section 3 how this shift arises owing to the separation between the frequency of maximum growth and the frequency where E_1/B_1 is smallest. The magnitude of E_1/B_1 for the fundamental when averaged over the half width of the peaks shown in E_1 and B_1 is $3.3c$ or 10^9 m s^{-1}. This value becomes larger (more electrostatic) by $\sim$30% for each successive harmonic above the fundamental.

2.3. Electron Distributions and Modeling

[14] Since the field-aligned electron population in the aurora is continually being replenished, the electron distributions, if observed in the source region for the observed harmonic emissions, may be continuously unstable at the source altitude. For this reason the features leading to ion wave growth will be represented in the measured distribution.

[15] Figure 3 shows two examples of the electron distribution measured at times during the interval presented in Figure 1. Both are measured in the upward current region and at a time when FAST observes an ion beam, however, the first (Figure 3a) is from that time when harmonic waves are not observed, and the second (Figure 3b) is taken from that time when the emission of these waves is most intense. Both distributions are observed simultaneously with intense AKR emissions and are both potential source distributions for this type of radiation. The boundaries superimposed on the distribution mark the accessibility of particles from different sources to the different regions of phase space [*Chiu and Schulz*, 1978; *Delory et al.*, 1998]. These follow from conservation of magnetic moment in a field-aligned potential drop. The necessary potentials are determined from the characteristic energy of the electrons and ions at these times and are $\sim$1000 and 1100 eV, respectively. These lines essentially divide the distribution into three components including an adiabatically folded beam (shell) lying outside the ellipse and outside the loss cone in the upgoing direction, a population occupying an adiabatically forbidden region of phase space inside the ellipse and outside the inner portion of the loss cone hyperbolae (trapped), and a component presumably comprised of primary and secondary electrons backscattered from the ionosphere falling within the ellipse and loss cone hyperbolae.

[16] The distribution function in Figure 3a shows most of the features expected of a distribution thermalized through
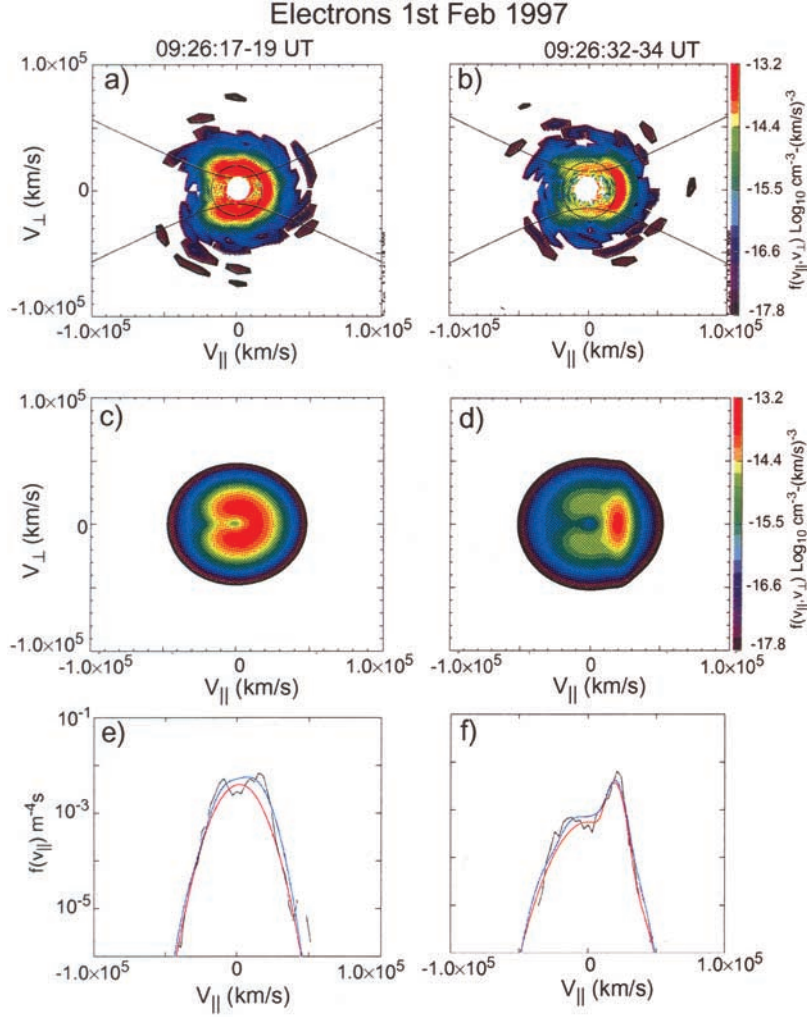
Figure 3. (a, b) 80 ms snapshots of the observed distribution function at times when harmonic emissions are not observed (Figure 3a) and when they are (Figure 3b). Positive $v_{\parallel}$ here indicates the downward or earthward field-aligned direction. (c, d) Models based on equations (1)–(3) and the parameters in Table 1. (e–f) Reduced distributions. The black lines are the reduced observed distributions (from Figures 3a and 3b); the blue lines are the reduced model distributions (from Figures 3c and 3d), while red lines correspond to reduced and fitted multiple component bi-Maxwellians.

the emission of AKR [*Pritchett et al.*, 1999, Figure 3] with diffusion of the shell into the trapped and loss cone regions of velocity space. Similar features are less apparent in Figure 3b with the most striking difference being the presence of the field-aligned beam. The angular width of the beam suggests a much lower source altitude for these electrons or that the majority of the potential drop occurred not far above the spacecraft.

[17] To reproduce the properties of the observed distribution we employ a three-component electron distribution function consisting of an adiabatically folded beam of the form

$$f_s(v_\perp, v_\parallel) = N_s \left(\frac{v_\perp^2 + v_\parallel^2 + C^2}{v_s^2} \right) \exp\left[-\frac{v_\perp^2 + v_\parallel^2}{v_s^2} \right]$$
$$- N_l \exp\left[-\frac{v_\perp^2 + (v_\parallel - v_{ol})^2}{v_l^2} \right], \quad (1)$$

a "trapped" population (which is basically a double-sided loss cone) expressed as a subtracted Maxwellian of the form

$$f_s(v_\perp, v_\parallel) = N_t \exp\left[-\frac{(v_\parallel - v_{ot})^2}{v_{\parallel t}^2} \right] \left\{ \left(1 + \frac{\alpha\beta}{(1-\beta)} \right) \exp\left[-\frac{v_\perp^2}{v_{\perp t}^2} \right] \right.$$
$$\left. - \frac{\alpha}{(1-\beta)} \exp\left[-\frac{v_\perp^2}{\beta v_{\perp t}^2} \right] \right\}, \quad (2)$$

and a cold field-aligned electron beam represented as an anisotropic bi-Maxwellian,

$$f_b(v_\perp, v_\parallel) = N_b \exp\left[-\frac{(v_\parallel - v_{ob})^2}{v_{\parallel b}^2} \right] \exp\left[-\frac{v_\perp^2}{v_{\perp b}^2} \right], \quad (3)$$

where $N_s = n_s / [v_s \pi^{3/2}(C^2 + 3v_s^2)]$, $N_{1c} = n_{1c}/(\pi v_{1c})^{3/2}$, and $N_t = N_b = n_b/(\pi^{3/2} v_{\perp b}^2 v_{\parallel b})$. Here n_j is the number density, v_j is the thermal velocity for an isotropic component (i.e., $v_{\perp j} = v_{\parallel j}$),

Table 1. Model Parameters for the Electron Distributions Shown in Figures 3a and 3c (Stable) and Figures 3b and 3d (Unstable) and the Corresponding Ion Distributions[a]

Component	n, cm^{-3}		$T_{\perp j}$, eV		$T_{\parallel j}$, eV		v_{oj}, km s^{-1}	
	Stable	Unstable	Stable	Unstable	Stable	Unstable	Stable	Unstable
Plasma sheet ions (*it*)	0.21	0.21	4,500.0	4,500.0	4,500.0	4,500.0	0	0
Ion beam (*ib*)	0.21	0.21	1,300.0	1,300.0	260.0	260.0	700	700
Electron shell (*es*)	2.5	0.323	700.0	700.0	700	700.0	0	0
Electron loss cone (*el*)	−0.15	−0.015	600.0	500.0	600	300.0	−16,000	−17,500.0
Electron beam (*eb*)	0.0	0.1	UD	700.0	UD	100.0	UD	19,500.0
Trapped electrons (*et*)	0.15	0.0	300.0	UD	600.0	UD	0.0	UD

[a] The letters in parentheses refer to the subscripts by which they are identified in the text and the functional form used to model each from equations (1)–(3). The "UD" signifies an undefined value for a zero density component. The temperature of the plasma sheet ions is taken from the thermal velocity under the assumption of a Maxwellian. When represented by equation (2) with $\alpha = \beta = 1$, this velocity is multiplied by $\sqrt{2}$ to give $v_{\perp it}$ $\beta_{\perp it}$ is the plasma beta for plasma sheet protons based on their perpendicular temperature, and V_A is the Alfven speed.

and C is a constant necessary to avoid negative phase space densities due to the subtraction of the second term in (1). The second-order perpendicular velocity moment of (2) is $\langle v_\perp^2 \rangle = v_{\perp t}^2(1 + \alpha\beta)$, where α and β can be thought of as parameters representing the depth and width of a double-sided loss cone. Throughout this study we set $\alpha = \beta = 1$. By combining these three component distributions the essential features of the observed distribution can be modeled as a sum of functions separable in $v_\parallel$ and $v_\perp$. This significantly simplifies the treatment of the velocity integrals involved in solving the dispersion relation since the well-known plasma dispersion function [*Fried and Conte*, 1961] can be used directly. The elements of the dispersion tensor associated with each of these components are given in Appendix A.

[18] By fitting these functional forms to the observed distributions we obtain a model for the plasma accurate at least over the sampling period of the detectors (80 ms) to yield the parameters given in Table 1. Each component in the plasma as shown in Table 1 is identified throughout this report by a two-letter subscript. The first specifies the species i.e., ions "i" or electrons "e", while the second identifies the functional form used to model this component from (1)–(3), i.e., shell "s", loss cone "1", trapped "t", or beam "b". Using this approach, the electron beam component has the subscript "eb", the shell electrons have the subscript "es", the loss cone electrons have the subscript "el", the trapped electrons have the subscript "et", the plasma sheet ions have the subscript "it", and the ion beam has the subscript "ib." The trapped electrons are secondary electrons backscattered from the ionosphere or electrons diffused from the shell and are trapped between the auroral potential at the high-altitude end and the geomagnetic field at lower altitudes. The "trapped" ions, however, are of plasma sheet origin and are trapped on geomagnetic field lines between hemispheres. The subscript "o" represents a beam or drift velocity; in the absence of this subscript then all velocities referred to are thermal velocities. When discussing the interaction of each component with waves of a given frequency ω and parallel wave number $k_\parallel$, a useful heuristic for discussing the strength or resonance in a multiple component hot plasma is to normalize the resonance condition in terms of the thermal velocity of the component under consideration as $Re(\zeta_j) = [Re(\omega) - k_\parallel v_{oj} - n\Omega_j]/k_\parallel v_j$. This is the real part of the argument of the plasma dispersion function which appears in Appendix A. When this expression has values less than 1, then we have a strongly resonant wave-particle interaction; for values greater than 1, then we have a weakly resonant interaction; and for values very much larger than 1, the interaction is nonresonant.

[19] The fits to the distribution functions are performed using a nonlinear least squares fitting approach. The observed electron distributions from which the parameters of Table 1 are derived are shown in Figures 3a and 3b, and the corresponding fitted electron distributions are shown in Figures 3c and 3d. The goodness of fit for parallel growing instabilities is demonstrated by Figures 3e and 3f, which show the reduced observed distribution function (black lines), the reduced distribution function from a two-component bi-Maxwellian model, and the reduced distribution from the models shown in Figures 3c and 3d, (blue lines) obtained by integrating over perpendicular velocities. Both the bi-Maxwellian and shell model fits to Figure 3a do not exhibit appreciable $df/d|v_\parallel| > 0$, and the distribution is stable to parallel growing instabilities. The dip in the middle of the reduced distribution in the data is primarily due to the subtraction of electrons with energies below 100 eV to remove photoelectrons and in reality would appear more as the blue line suggests. The reduced distribution shown in Figure 3f, however, clearly shows $df/d|v_\parallel| > 0$. The fit to the beam for both the bi-Maxwellian and shell case has the same temperature of 100 eV and drift of 20,000 km s^{-1}, yielding $v_{oeb}/v_{eb} = 3.37$. For the shell electrons the temperature is 700 eV, and for the bi-Maxwellian plasma sheet electrons the temperature is 1070 eV with total densities of 0.423 and 0.36 cm^{-3} respectively.

3. Wave Dispersion

[20] In this section we discuss only those wave modes that are important for understanding the observed wave emissions at Ω_p and its harmonics. For this reason we do not include dispersion results for the whistler mode nor the L, X ion cyclotron mode as discussed by *Temerin and Lysak* [1984]. For a more complete discussion of wave dispersion at extra low frequencies the interested reader is referred to *Andre* [1985b].

3.1. Mode Identification

[21] Figure 4a shows a three-dimensional view of the dispersion surfaces calculated for the parameters given in Table 1. The green surface includes the dispersion surfaces for ion cyclotron waves at and between harmonics of Ω_p, while the black, blue, and maroon surfaces show the

extension of each of the fundamental and first and second harmonic surfaces to larger $k_\parallel$. The evenly sloped purple surface in the background is well described by the dispersion relation $\omega = (1/2)k_\parallel v_{oeb}$ at perpendicular wave numbers up to $k_\perp \rho_{it} = 1$, where ρ_{it} is the gyroradius of the plasma sheet ions. To aid in visualizing the mode structure, Figure 4b presents a slice through the surfaces along $k_\parallel$ taken at $k_\perp \rho_{it} = 1$ and reveals in more detail the dispersion topology at the perpendicular wavelengths, where ion cyclotron instability can be expected. The green surface corresponds to the most steeply sloped portion of the dispersion curves and approaches $n\Omega_p$ from above as $k_\perp \rho_{it}$ goes to zero. This portion of the wave dispersion has been described previously by the work of *Fredericks* [1968], where the cutoffs and resonances at each harmonic arise through thermal effects. The more gently sloping curve corresponds to the purple surface and also exhibits cutoffs and resonances at multiples of Ω_p. As the beam velocity is increased and beam density and temperature decreased, the dispersion of this surface approaches $\omega = k_\parallel v_{oeb}$, and we recover the beam-plasma mode discussed by *Singh et al.* [1985]. However, if the beam density is increased at the expense of the shell component, the dispersion for this surface becomes ion acoustic like and can be described by $\omega = k_\parallel v_{cs}$ (in the limit where $k_\parallel \lambda_D \ll 1$), where v_{cs} is the ion acoustic speed, as discussed by *Bergmann* [1984]. This is shown in Figure 5, where the beam velocity and temperature are held fixed, but the beam density is reduced. For beam densities less than 1% of the total density the wave dispersion very nearly approaches $\omega = k_\parallel v_{oeb}$ (dash-dotted line). Whereas if all the density is contained in the drifting component, we recover the ion acoustic wave, and the wave phase speed falls toward the acoustic speeds of the beam component (dotted line) at $k_\perp = 0$. In Figure 5 we are at $k_\perp \rho_{it} = 1$, and so the wave phase speed does not quite reach the acoustic speed of the beam. For the plasma environment under consideration here we call this wave the intermediate beam-plasma mode of which the ion acoustic and beam-plasma modes are limits. At parallel wave numbers smaller than those at which this surface intersects the ion cyclotron wave surfaces, the ion cyclotron instability driven by Landau resonance with the electron beam may occur. Beyond $k_\perp \rho_{it} = 1$ this surface steepens and becomes increasingly difficult to follow as it finds its way through the proton harmonic surfaces.

3.2. Temporal Growth Rates

[22] Since we are in a regime where for the majority of the plasma, $T_i \gg T_e$, the ion acoustic instability (remember that the threshold drift for the ion acoustic instability is $v_{oeb} > v_{cs}$ and $v_{cs} > v_{\text{ions}}$ in this regime; where v_{cs} and v_{ions} are the ion acoustic and ion thermal speeds, respectively) requires a much higher electron drift speed than the ion cyclotron instability, and the threshold drift for both instabilities approaches v_{eb} [*Kindel and Kennel*, 1971]. This also applies for the beam-plasma mode, which behaves in a way similar to the ion acoustic instabilities with increasing ion Landau damping as T_i is increased. For this reason, and the electron Landau damping provided by the electron shell at large pitch angles, the solution of the dispersion relation, $D(\omega, k) = 0$, for the distribution shown in Figure 3a indicates that the plasma is stable in the range of $n\Omega_p$ and also between each harmonic. For the distribution shown in
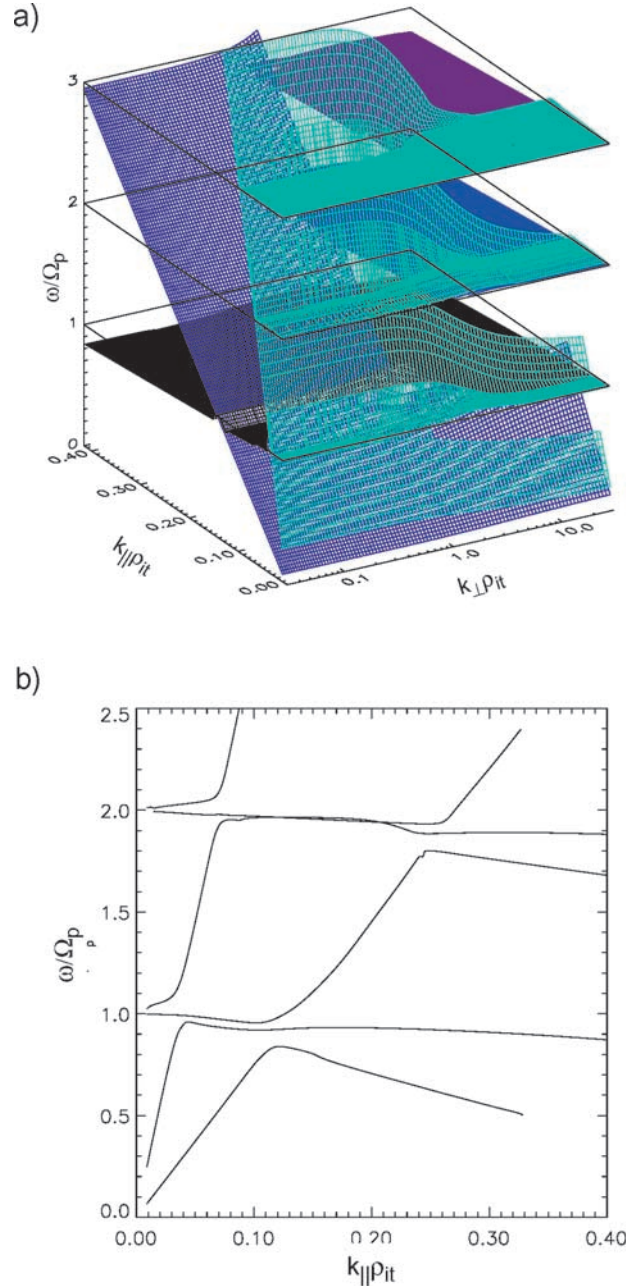

Figure 4. (a) Dispersion surfaces calculated for the parameters given in Table 1. See text for a detailed explanation. (b) A slice through the dispersion surfaces at $k_\perp \rho_{it} = 1$.

Figure 3b, however, the drift speed of the beam exceeds its own thermal speed and also that of the shell component. Furthermore, the total distribution is strongly peaked at $v_\parallel = v_{oeb}$ and $v_\perp = 0$. These features allow the wave growing on the positive slope of the beam to overcome the damping associated with the shell electrons at larger pitch angles. For the given parameters, waves at the first three ion cyclotron harmonics are unstable with perpendicular wavelengths of the order of the average plasma sheet ion gyroradius for the fundamental and somewhat larger for each harmonic there after. In addition, the intermediate beam-plasma mode is also excited, which is less subject to ion Landau damping
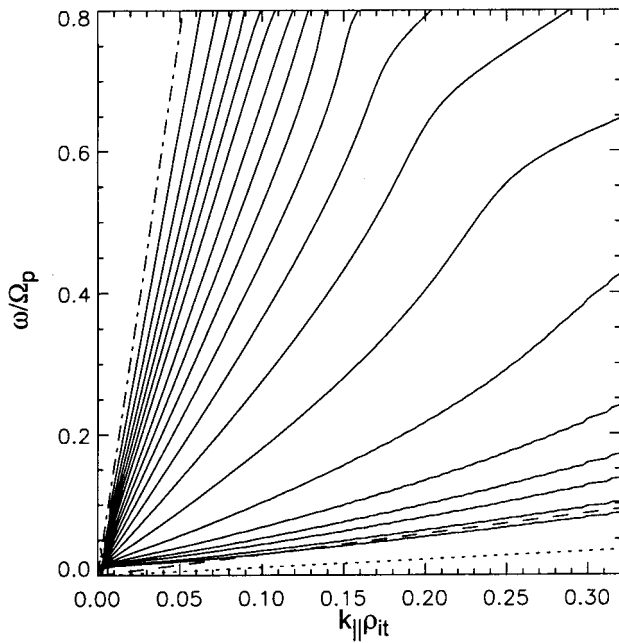
Figure 5. Variation in the dispersion of the intermediate beam-plasma mode for changing relative electron beam densities from 100% (lowest phase speed) to 1% (highest phase speed) of the total plasma density at $k_\perp \rho_{it} = 1$ in steps of 10% down to 80% and 5% thereafter. The dotted line is the ion acoustic speed based on the temperature of the cool electron beam, while the dashed line is that based on the temperature of the electron shell. The dash-dotted line is the electron beam speed, v_{oeb}.

than the ion acoustic wave since its phase speed (in this case ~4 times the ion acoustic speed) is significantly larger than the plasma sheet ion thermal speed.

[23] Figures 6a and 6b show the unstable wave surface and growth rate for the intermediate beam-plasma wave and fundamental ion cyclotron wave, respectively. The former grows at frequencies between and through the harmonics at oblique angles up to $k_\perp \rho_{it} = 1$. For the parameters chosen this mode is increasingly subject to ion Landau damping with increasing $k_\parallel/k_\perp$ by hot plasma sheet protons, so that maximum growth for this mode occurs at $2.2\Omega_p$ and $k_\perp \rho_{it} = 0.07$ ($k_\parallel/k_\perp = 4.4$) (as indicated by the cross in Figure 6a). The parallel wave number at which maximum growth occurs is $k_\parallel = 0.3/\rho_{it}$, which is $\sim \omega_e/v_{oeb}$ as expected for the beam-plasma mode (or for the Buneman instability in the limit of a single drifting electron component). This mode excites broadband growth extending from almost zero frequency up to the fourth Ω_p harmonic.

[24] The most strongly growing wave, however, is that which has traditionally been identified as the electrostatic ion cyclotron wave. Growth is centered on Ω_p with phase speeds extending from just below the electron beam drift speed out to the point of coupling between the surfaces shown in Figures 6a and 6b at roughly $0.5\ v_{oeb}$. This coupling is manifest in these plots by the tightly spaced contours in real frequency at $k_\parallel \rho_{it} = 0.03$ and 0.13. The unstable region covers a wide range of perpendicular wave numbers centered on $k_\perp \rho_{it} = 1$. For the unstable harmonics,

which are not shown here, the frequency of maximum growth occurs just below $n\Omega_p$. Since the parallel phase speed of these waves is of the order of one half the beam speed, and so less than the thermal velocity of the electron shell component (15,700 km s^{-1}, these waves are the so-called neutralized Bernstein modes as they allow electrons to flow along $\mathbf{B_0}$ to cancel charge separation.

[25] The neutralized ion Bernstein mode is also cyclotron resonant with the ion beam. The effects of this on the ion distribution can be clearly seen in Figure 1 as the spreading of the ion beam pitch angle where the wave activity is most intense. Since the magnitude of $k_\parallel v_{oib}$ is of the order of -10 Hz (since $k_\parallel$ and v_{oib} are oppositely directed), the Doppler shift is insufficient to take the beam ions completely out of cyclotron resonance, and ζ_{ib} is positive with a value ~ 1 at frequencies within 10% of Ω_p and approaches zero below Ω_p. For the ion and electron beam speeds given in Table 1, an increase in the ion beam density can significantly enhance the temporal growth rate particularly at frequencies just below Ω_p. Importantly, however, the instability still exists if there is no ion beam yet disappears in the absence of the electron beam. This shows that the ion beam is an additional source of free energy for the growing wave but is insufficient alone to overcome the Landau damping of the shell electrons and the cyclotron damping provided by the plasma sheet ions.

[26] An additional short-wavelength perpendicular electrostatic mode occurs at multiples of Ω_p supported by the ion beam protons at $k_\perp \rho_{it} \sim 3$ or $k_\perp \rho_{ib} \sim 1$. This mode is driven by the proton loss cone and is a pure ion Bernstein mode, unstable at several harmonics of Ω_p and continues growing at values of $n\Omega_p$, where the traditional electrostatic (now electromagnetic) ion cyclotron instability for the neutralized Bernstein mode as discussed above is stable. A similar wave mode has been discussed by *Andre et al.* [1986]. It occurs at parallel wave numbers and frequencies approximately satisfying $\omega - k_\parallel v_{oib} - \Omega_p = 0$ and occurs almost exactly on Ω_p for typically observed ion beam drift speeds. The wave becomes increasingly unstable with the increasing density in the proton loss cone distribution and also with small increases in ion beam speed from the values given in Table 1; however, the instability still exists when $v_{oib} = 0$. As the ion beam density is increased above zero, the wave obtains additional free energy through cyclotron resonance with the ion beam for which ζ_{ib} is very close to zero. The interaction of the wave with the ion beam is very similar to that found for the neutralized ion Bernstein mode discussed above; however, the magnitude of the Doppler shift is significantly smaller with $k_\parallel v_{oib} \sim 1$ Hz. In the absence of the ion beam component (or at least a second ion component of this temperature) the mode does not exist at these perpendicular wave numbers, and if the ion loss cone is replaced by a bi-Maxwellian distribution, this mode becomes stable. The growth rate of this mode is also sensitive to the temperature of the electron shell component through electron Landau damping.

[27] One of the outstanding issues associated with observation of these waves is the magnetic component present in the observations discussed in section 2.2. Figures 6c and 6d address this issue by showing the variation in the E_1/B_1 ratio as a function of $k_\perp \rho_{it}$ and $k_\parallel \rho_{it}$, where the grey scale again
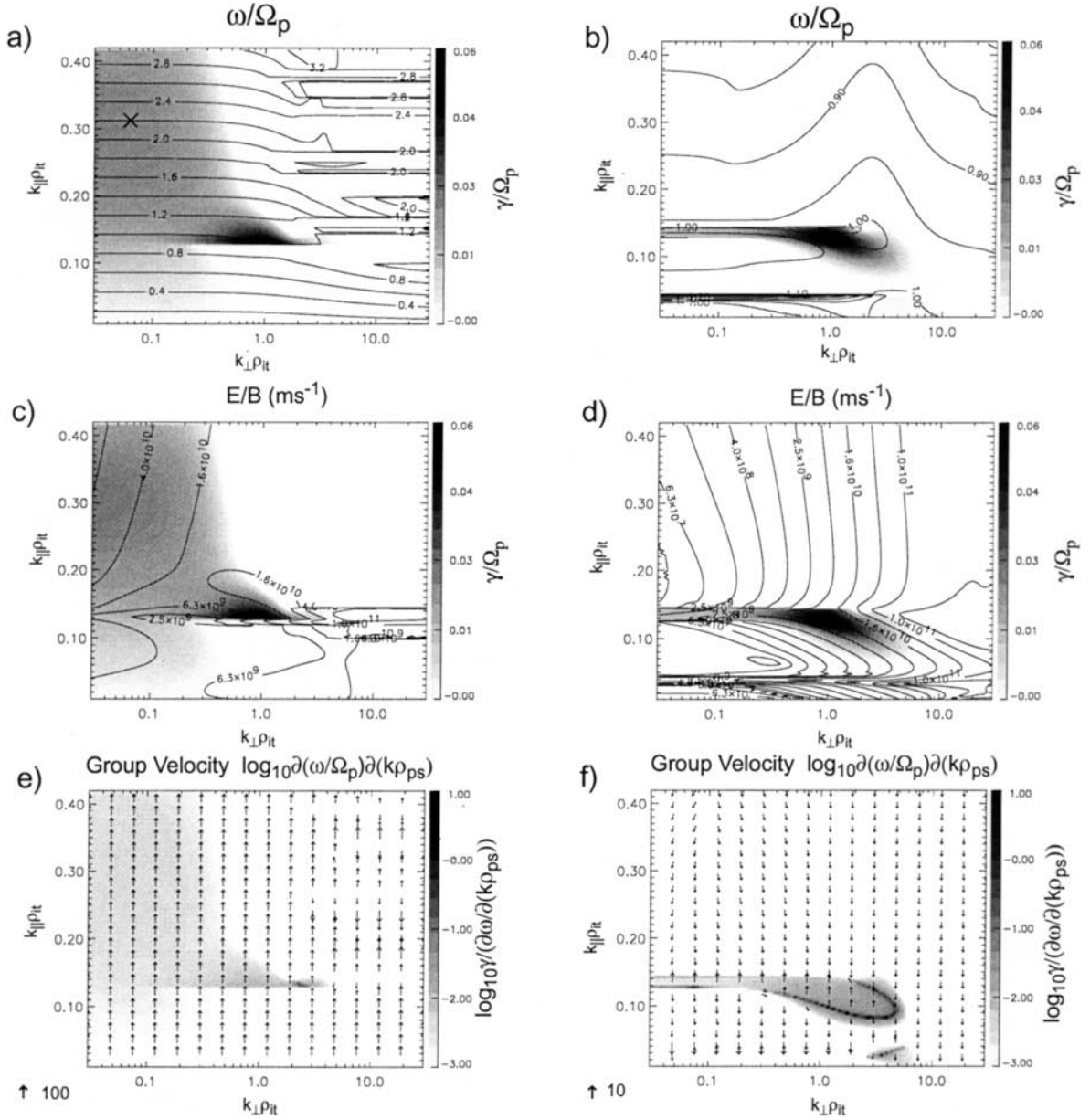
Figure 6. Contour plots of the dispersion surface corresponding to (a, c, and e) the intermediate-beam plasma surface and (b, d, and f) fundamental proton cyclotron surface. (a, b) The real frequency (contours) and temporal growth rates (grey scale). (c, d) The value of the ratio E_1/B_1 (contours) and the temporal growth rate (grey scale). (e, f) The wave group velocity (arrows) and convective growth rates (grey scale). The units for each quantity except in the case of E_1/B_1 are normalized and as given on each plot. The magnitude of the group velocity is related logarithmically to the length of the arrows; that is, an arrow half the length of the maximum length arrow indicates a velocity 2 orders of magnitude smaller.

corresponds to the growth rate. Not surprisingly, the relevant wave surface shown becomes increasingly electromagnetic with decreasing $|\mathbf{k}|$. The exceptions to this general pattern occur in the vicinity of Ω_p on the beam-plasma mode surface. At the point where the beam mode surface couples to the ion cyclotron surface, there is a kink in the E_1/B_1 contours that for parallel wave numbers less than $k_{\parallel}\rho_{it} = 0.15$ (or for phase speeds greater than 0.5 v_{oeb}) reduces E_1/B_1 by up to an order of magnitude. At maximum temporal growth, $E_1/B_1 = 6.0e9$ m s^{-1} with this ratio

extending from 6.0×10^7 to 2.5×10^{11} over the range of unstable wave numbers. While this covers the range of E_1/B_1 ratios observed for these waves, maximum temporal growth occurs with E_1/B_1 ratios almost an order of magnitude higher than those typically observed. Furthermore, the pure ion Bernstein mode identified at $k_{\perp}\rho_{it} = 3.0$ cannot be the source of the magnetic component, since at maximum temporal growth this wave is electrostatic with maximum growth occurring with $E_1/B_1 = 6.0 \times 10^{10}$. The resolution of this issue lies in the lower E_1/B_1 ratio found where the

convective growth rate (γ_c) of the neutralized ion Bernstein mode is greatest.

3.3. Convective Growth Rates

[28] Figures 6e and 6f show the group velocity vectors and the convective growth rates for both dispersion surfaces. Vectors having field-aligned components parallel to the electron beam and the magnetic field direction point upward, while antiparallel components point downward. For all waves shown the phase velocity is in the field-aligned direction or in the same direction as the electron beam. As expected, the beam-plasma mode has a group velocity that points everywhere in the beam direction and is a forward propagating wave in the sense that its group velocity and phase velocity have components pointing in the same direction along $\mathbf{B}_0$. This wave propagates down the field line toward the ionosphere with group speed very similar to the wave phase speed of 0.5 v_{oeb} (10,000 km s^{-1}) except where $w/\Omega_p - > 1$ and $k_\perp \rho_{it} - > 1$ and in the broken area for the largest $|\mathbf{k}|$ values shown. The group velocity is very closely aligned with the field-aligned direction, so wave propagation out of the side of the electron beam region is unlikely, at least in the homogeneous model considered here. The convective growth rates shown by the grey scale have a maximum value of 1.0×10^{-4} m^{-1} in the region of coupling. This yields a parallel e-folding distance of $\sim$27 km. The observed amplitudes of $10-100$ mV m^{-1} for these broadband emissions requires $5-10$ e-fold from noise levels [*Temerin and Lysak*, 1984], indicating source regions of greater than 100 km.

[29] For the proton harmonic surface, convective growth rates are significantly larger. In this regime the instability grows on a flat portion of the dispersion surface and for both forward and backward propagating waves. This allows for both downward and upward Poynting fluxes, respectively, along the field line and accounts for the Poynting flux observations reported by *Chaston et al.* [1998]. This dispersion also provides a narrow region of k-space where the group velocity goes to zero and thus yields a singularity in the convective growth rate or absolute instability ($\gamma_c - > \infty$) that, with reference to Figure 4b, occurs very close to Ω_p. Around this singularity the growth remains field-aligned, and the E_1/B_1 ratio is as small as 1.0×10^8 m s^{-1}. Given the combination of large temporal and convective growth it seems possible that these linear results can account for the large amplitude of the observed emissions discussed earlier and the large magnetic component. The "natural line width" of the emission (frequency range over which the temporal growth γ is greater than zero) is $\sim$66 Hz; however, the fact that the singularity in γ_c occurs at Ω_p effectively allows the growth of a highly narrowbanded emission at this normalized frequency over the range of altitudes where the instability occurs as observed. In this case the observed spectral width in the spacecraft frame is largely due to Doppler broadening. For a spacecraft velocity perpendicular to the magnetic field of 5 km s^{-1} and from the modeled unstable wave numbers, we have perpendicular wavelengths down to $\sim$400 m, thereby providing $\sim$13 Hz added spectral width. The observed width of the fundamental shown in Figure 2 at half maximum height is $\sim$30 Hz.

[30] Furthermore, since maximum convective growth occurs at the point of coupling between the branches of the intermediate beam plasma modes across Ω_p, the large growth occurring close to this frequency is robust for a wide range of parameters. The solid line in Figure 7a shows the variation of this frequency with beam energy for fixed v_{oeb}/v_{eb}. While the energy of the beam ranges from 250 eV up to 5 keV, the wave frequency at which maximum convective growth occurs varies by less than 10% on either side of Ω_p. All our events have beam energies greater than 1 keV, and over that energy range the frequency of maximum γ_c is within 4% of Ω_p. The maximum temporal growth rate (indicated by the dashed line) for the most energetic beam at 5 keV occurs at $1.1\Omega_p$ and falls below Ω_p for energies less than 1 keV.

[31] Since the E_1/B_1 ratio varies over the region of unstable frequency space, it cannot be expected that the spectral peaks in E_1 and B_1 will occur at the same frequency or necessarily exactly where maximum temporal or convective growth occur. In Figure 7a it can be seen that the observed frequency of the fundamental for the electric (asterisks) and magnetic (diamonds) fields are separated and by up to 5% of the proton gyrofrequency with greatest separation occurring at the extremes of the energy range shown here. The frequency of the spectral peak in the electric field lies between that predicted from maximum temporal and convective growth while the magnetic peak falls just below that predicted at maximum convective-growth. This pattern is that expected from the contour plot shown in Figure 6d that indicates that the waves become more electrostatic with increasing frequency. This is demonstrated in Figure 7b, which shows that E_1/B_1 values calculated at the frequency of maximum convective growth are an order of magnitude smaller than that found at the frequency of maximum temporal growth. The scatter of measured E_1/B_1 ratios indicated by the plus signs on this plot fall more closely around the calculated E_1/B_1 ratio at maximum γ_c (solid line) than those E_1/B_1 values calculated at maximum temporal growth rate (γ) (dashed line). In general, Figure 7b shows that the wave becomes more magnetic with increasing beam energy as the Landau resonance occurs at smaller $k_\parallel$. Above a beam energy of 800 eV the predicted and observed ratios of E_1/B_1 can be seen to decrease together to values as low as c with increasing beam energy. In fact, the whole range of observed frequencies and E_1/B_1 ratios shown in Figure 7 fall within the range predicted. Furthermore, comparison of Figures 7a and 7b shows that the most strongly magnetic waves occur where the wave frequency of maximum γ_c is closest to Ω_p.

4. Electron Beams With Velocity v_{oeb} Greater Than the Thermal Speed v_{eb}

[32] It is well known that when the relative drift between an electron and ion component in a plasma exceeds the thermal speed of the electron component, then effectively the entire electron distribution can contribute nonresonantly to the instability, resulting in the violent broadband wave growth called the Buneman instability. In the model presented above, $v_{oeb}/v_{eb} = 3.3$ for the electron beam component. So, given that the ion components are either stationary (plasma sheet) or counterstreaming (ion beam) with the electron beam, the threshold for the Buneman instability or
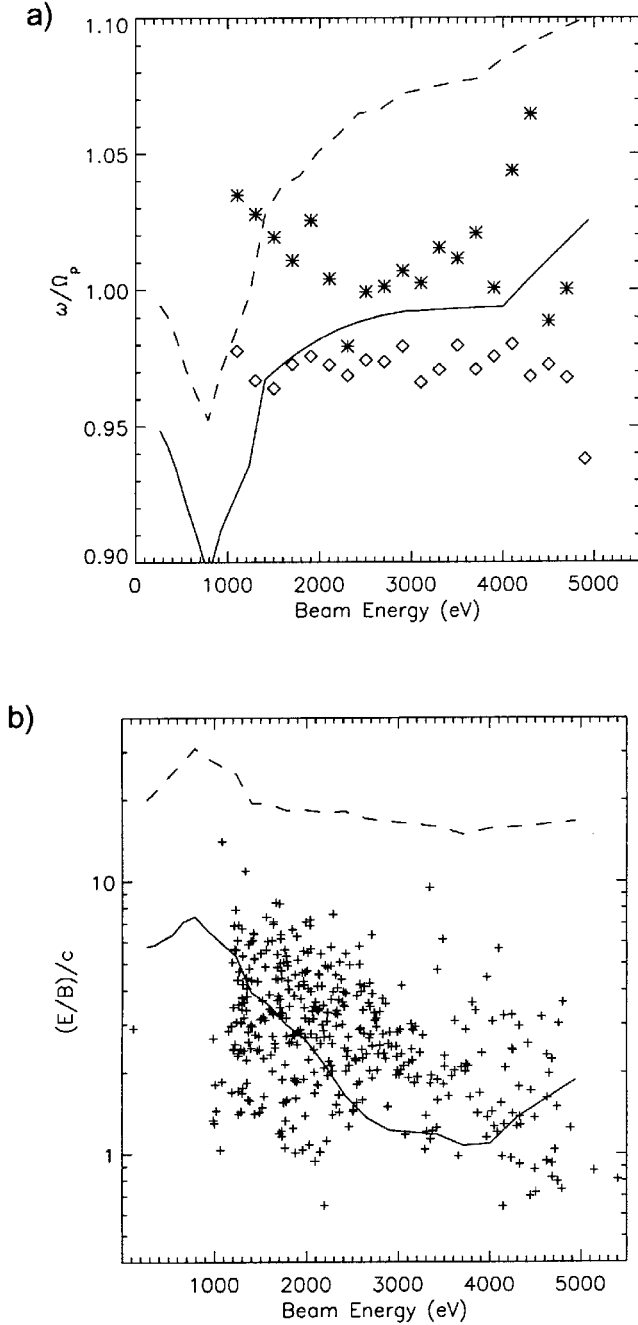
a)

b)

Figure 7. (a) Frequency of maximum temporal (dashed) and convective (solid) growth rates at $k_\perp \rho_{it} = 1$ as a function of electron beam energy. The asterisks and the diamonds indicate the average wave frequency (as shown on the y axis) observed for the electric and magnetic field fluctuations, respectively, at the electron beam energy shown on the x axis. These results are based on the data from Figure 1b. E_1/B_1 at maximum temporal (dashed) and convective (solid) growth rates at $k_\perp \rho_{it} = 1$ as a function of electron beam energy. The plus signs indicate the observed values of E_1/B_1.

more correctly, for the two-electron component mode used here, the strong beam-plasma instability is exceeded. However, owing to the combined effects of the Landau damping provided by the adiabatically folded plasma sheet electrons

or shell and plasma sheet ions, the instability does not occur until larger drift speeds and/or cooler electron populations are employed. In fact, the damping provided by the shell is such that the plasma is stable at Ω_p for $v_{oeb}/v_{eb} < 2.3$.

[33] Figure 8a shows the variation of the wave spectra with decreasing electron beam temperature at $k_\perp \rho_{it} = 1$ covering v_{oeb}/v_{eb} from 3.1 up to 8.4. At $v_{oeb}/v_{eb} = 3.1$ a single growing wave at Ω_p exists. As the beam cools, instability also occurs at $2\Omega_p$. Then for lower beam temperatures or greater v_{oeb}/v_{eb}, progressively the harmonic structure is removed as the harmonic electrostatic ion cyclotron wave surfaces become coupled, and nonresonant growth fills in the gaps in frequency between the resonances with waves on the intermediate beam-plasma mode surface. Effectively, the coupling between the branches of the beam-plasma mode across the cutoffs and resonances occurring at $n\Omega_p$ becomes more complete, so that a single mode without a observable stop band exists. The wave phase speed, however, does not alter greatly, and waves on this surface still roughly obey $\omega = 1/2 k_\| v_{oeb}$. For large enough v_{oeb}/v_{eb} we also find wave growth occurring at frequencies below Ω_p on the intermediate beam-plasma mode surface, so that eventually unstable frequencies extend from zero and over several harmonics of Ω_p. At threshold, growth of the intermediate beam-plasma mode occurs only at $k_\perp = 0$; however, as v_{oeb}/v_{eb} is increased, growth extends to larger $k_\perp$. Figure 6a shows that at $v_{oeb}/v_{eb} = 3.3$, broadband growth extends almost to wave numbers where the discrete ion cyclotron modes occur (i.e., the perpendicular wave number at which Figure 8 is plotted). For $v_{oeb}/v_{eb} > 4.3$, continuous growth occurs between the first two harmonics although peaks are still apparent at these frequencies. With sufficiently large v_{oeb}/v_{eb} the growth rate exceeds the cyclotron frequency even at $k_\perp \rho_{it} = 1$, and the ions become demagnetized, so that the harmonic structure disappears completely with growth rate increasing with decreasing $k_\perp$ and increasing $k_\|$ up to $\sim \omega_{pe}/v_{oeb}$. At this point we have a Buneman-like instability (in that the whole electron beam contributes to wave growth) with the wave dispersion of the intermediate beam-plasma mode.

[34] Several factors tend to retard the excitation of the nonresonant portion of the instability. The most obvious of these is the increase of the ion temperature. While the intermediate beam-plasma mode is much faster than the ion acoustic speed with a phase speed of $\sim$10,000 km s^{-1}, its growth is still significantly affected by the density and temperature of the hot plasma sheet component, which in this case has a thermal velocity of 1313 km s^{-1}, providing ion Landau damping for this wave in the tail (ζ_{it} for this wave is $\sim$7). However, the most important component in the model for stabilizing the broadband growth is the shell or adiabatically folded and accelerated plasma sheet component. For this component, ζ_s is less than 1, and the phase speed of the wave is very close to the thermal velocity of the shell. Waves at the harmonics of Ω_p occur at somewhat faster phase speeds since they more nearly obey $\omega = k_\| v_{oeb}$ and so are less subject to damping by the plasma sheet electrons than those waves occurring on the intermediate beam-plasma dispersion surface.

[35] It is the detailed form of the electron distribution function that really prevents broadband growth and very large temporal growth rates. Figure 8b shows the spectrum
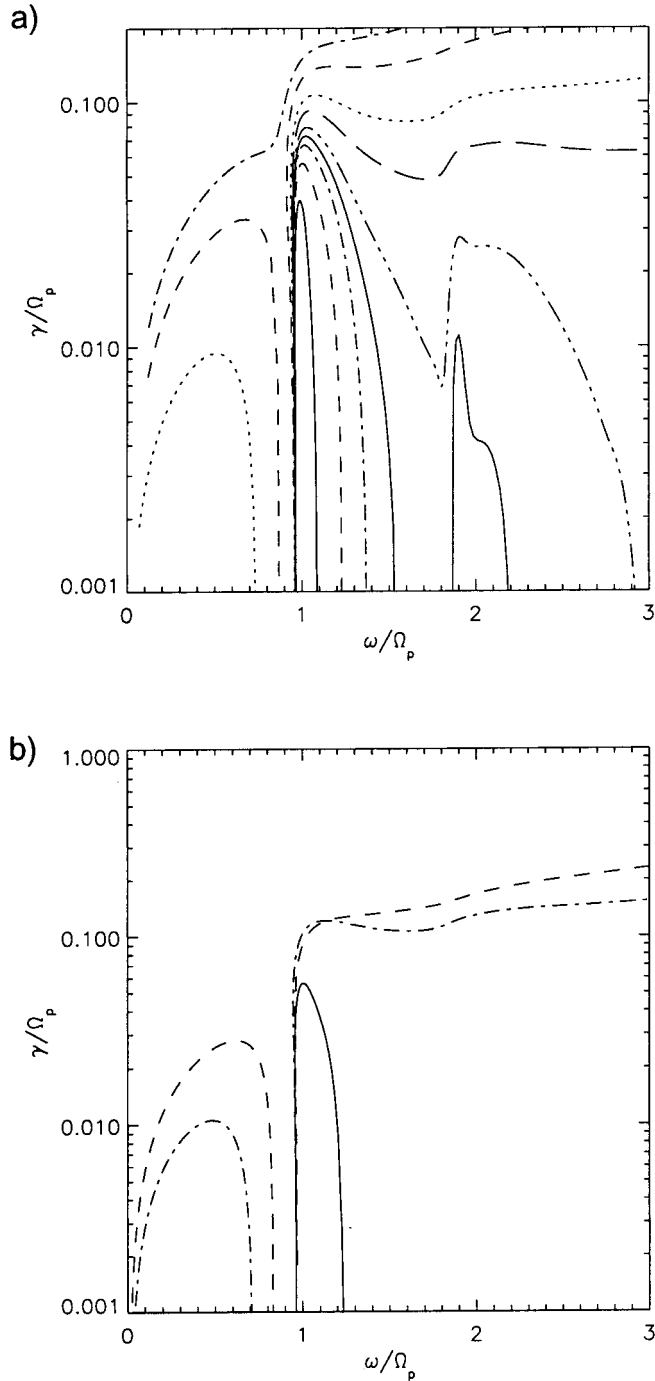
a)

b)

Figure 8. (a) Growing wave spectra for differing values of the v_{oeb}/v_{eb} with v_{oeb} held fixed at the value given in Table 1 (19,500 km s^{-1}) at $k_{\perp}\rho_{it} = 1$. The narrowest solid line peak at $\omega/\Omega_p = 1$ represents wave growth for the ratio $v_{oeb}/v_{eb} = 3.1$, and successive lines moving outward represent growth rates for $v_{oeb}/v_{eb} = 3.3, 3.4, 3.47, 3.53, 3.66, 3.81, 4.17$, and 4.67. Growth below $\omega/\Omega_p = 1$ is first seen for $v_{oeb}/v_{eb} = 3.81$ at this wave number. (b) Growing wave spectra when the model includes the adiabatic shell component with $T_{es} = 700$ eV as defined in Table 1 (solid line) and when this component is replaced by a Maxwellian with temperatures of 700 eV (dashed line) and 1100 eV (dash-dotted line).

at $k_{\perp}\rho_{it} = 1$ for the plasma sheet electrons modeled as a Maxwellian with temperatures 700 and 1100 eV and as an adiabatically folded shell of temperature 700 eV. A temperature of 1100 eV is found for the fitted Maxwellian to the distribution shown in Figure 3f, while 700 eV is the temperature of the shell. The reduced form of the electron distribution shown in Figure 3f looks very similar for each functional form modeled; however, the stability of each in the range of ion frequencies is distinctly different. Figure 8b shows that the Maxwellian plasma sheet electron component at both temperatures leads to broadband growth extending from zero frequency and continuing smoothly through the harmonics of Ω_p except just below the proton Ω_p, where a stop band exists. In contrast, at this perpendicular wave number the shell provides a single peak in the spectrum at Ω_p. This is associated with the integral over the Landau resonance condition, which in the case of the shell has a much larger contribution from negative $\partial f/\partial v_{\parallel}$ for any slice along $v_{\parallel}$ than for a simple drifting bi-Maxwellian or nondrifting isotropic plasma sheet component. The modeling of the electrons in this manner is essential for reproducing the observed wave spectra for the observed electron drift speeds without exciting violent broadband growth. In fact, without the addition of the cool beam the adiabatically folded beam or shell is stable to both instabilities on the intermediate beam-plasma mode surface and instabilities on the electrostatic ion cyclotron wave surfaces despite the fact that the current through the plasma exceeds the threshold for the current driven instability. This allows a much larger current to be carried by the plasma before instability occurs and explains why, in Figure 1, no wave above Ω_p is observed until the cool field-aligned electrons are turned on.

5. Cold Plasma Effects

[36] Observations of AKR below the local electron gyrofrequency [*Delory et al.*, 1998], VLF wave dispersion [*Strangeway et al.*, 1998], comparisons of field-aligned currents from magnetometer measurements and energetic particle detectors [*Carlson et al.*, 1998], and considerations based on quasi-neutrality [*McFadden et al.*, 1999] have indicated the scarcity of cold plasma (<100 eV) above the auroral oval where upgoing ion beams exist and the cyclotron harmonic waves, which are the subject of this paper, are observed. These observations are the reason why a cold component was omitted from the model given in Table 1. We now investigate the effects of introducing a cold plasma component on the dispersion of these waves.

[37] Figure 9 shows the effect of adding 1 eV ion and electron components and progressively increasing their density on the dispersion of the fundamental resonance. The solid line, representing the wave real frequency at maximum growth, indicates just how sensitive the dispersion of the growing wave is to the presence of cold electron and ion components. The real frequency of the wave rapidly diverges from Ω_p as ion cyclotron damping here increases with the presence of cold nondrifting ions and moves well above Ω_p for cold plasma percentages exceeding 5%. With increasing cold plasma content the instability actually becomes broadband, and growth rates approach the proton
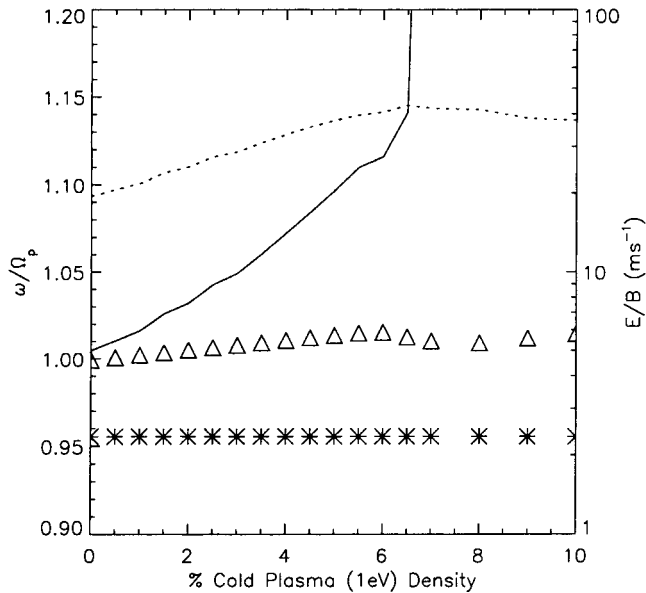
Figure 9. Cold plasma effects. Solid and dotted lines show the real frequency and E_1/B_1 values for increasing proportions of cold plasma content (1 eV ions and electrons), respectively, at maximum temporal growth rate and $k_\perp \rho_{it} = 1$. The asterisks and triangles show the same information at maximum convective growth and $k_\perp \rho_{it} = 1$.

cyclotron frequency since we now effectively have a two-stream/Buneman instability where, for this case, two cold electron and ion components stream by one another at speeds many times greater than their thermal speeds. There is little change in the frequency of maximum convective growth (indicated by asterisks) and in the corresponding E_1/B_1 ratio; however, the temporal growth at this frequency decreases with increasing cold plasma density to levels where the convective growth rate may have little meaning. It would seem then that for consistency between observations and linear Vlasov theory, there is virtually no cold plasma in the regions where the harmonic waves grow.

6. Discussion

[38] Observations from the FAST spacecraft's suite of instruments have removed much of the uncertainty regarding plasma parameters in the auroral acceleration region. As a result, significantly more rigorous tests of the ability of the linear Vlasov theory to predict observed wave characteristics from observed ion and electron distributions can be performed. With this in mind in this work we have examined the growth of electromagnetic cyclotron harmonics from an electron beam containing 25% of the total electron density whose drift velocity is several times larger than its thermal speed in a two-electron component plasma. This is a range of parameters thought unlikely to occur, owing to the inherent instability of the plasma under such conditions. In a bi-Maxwellian plasma such a configuration would proceed very quickly to saturation via heating the beam. Consequently, the range of electron drift speeds considered here differs from most others studied in association with ion waves in the aurora (*Bergmann* [1984], *Andre* [1985a],

Kauffmann and Kintner [1984], *Singh et al.* [1985], and many others).

6.1. Ion Acoustic Waves, Beam-Plasma Modes, and Electrostatic Ion Cyclotron Waves

[39] Here we digress to discuss where the wave modes studied in this report "fit in" with the similar wave modes considered by previous researchers. It was shown in section 3 how with decreasing beam density the wave dispersion changes from ion acoustic to beam-plasma-like, and hence we labeled the broadband waves generated as an intermediate beam-plasma mode. The ion acoustic and beam-plasma modes are essentially limits for the cases of very high and low relative beam density (n_b/n_o) as discussed by *Bergmann* [1984] and *Singh et al.* [1985], respectively. The former considered a three-component model where all the electron density was concentrated in the beam or drifting electron component with $v_{oe}/v_e < 1$. The latter present a model where the density of the beam is less than 3% of the total electron density, and $v_{oeb}/v_{eb} \gg 1$. Both models, however, generate broadband spectra for $k_\perp \rho_{it} < 1$ albeit with significantly different phase speeds. For the intermediate beam-plasma mode, which is the broadband wave identified in this study, a similar wave spectra prevails at these waves numbers. Furthermore, for both studies the waves occurring at $n\Omega_p$ and $k_\perp \rho_{it} \sim 1$ on the "electrostatic" ion cyclotron wave surfaces can, in fact, be followed to the parameter range found here, showing that they are indeed the same instability occurring for different drifting electron moments.

[40] The instability and resulting waves studied in this report are, however, distinct from those modeled by *Miura et al.* [1983], *Kauffman and Kintner* [1982] and *Okuda and Nishikawa* [1984], who invoke a Landau resonance with the ion beam as the source of free energy. Interferometric work by *Chaston et al.* [1998] indicates that the observed waves have perpendicular wavelengths up to ~1 km. Even under the electrostatic approximation this then provides parallel wave phase speeds several times faster than the ion beam velocity for reasonable values of $k_\perp/k_\parallel$. There are, however, some aspects of the observations that circumstantially may suggest Landau resonance with the ion beam. Firstly, *Chaston et al.* [1998] point out that the wave Poynting flux of the harmonic waves is often directed upward out of the oval. This suggests that the wave phase velocity will also be oriented in this direction, so that the wave cannot be Landau resonant with the electron beam. However, Figure 6f indicates that the wave may be backward propagating such that its phase and group velocities are in opposite directions. Consequently, a spacecraft flying above the source could see waves that are Landau resonant with the downgoing electron beam with upgoing Poynting fluxes and group velocities since the waves have both forward and backward propagating components.

6.2. Ion Heating

[41] The second aspect of the wave and particle observations that has suggested the ion beam as the free energy source for the waves has been the observed pitch angle diffusion and heating of the beam ions in the wave field. The pitch angle diffusion of the beam ions, shown in Figures 10a and 10b, is in appearance similar to that modeled by *Miura et al.* [1983] for ion waves inversely
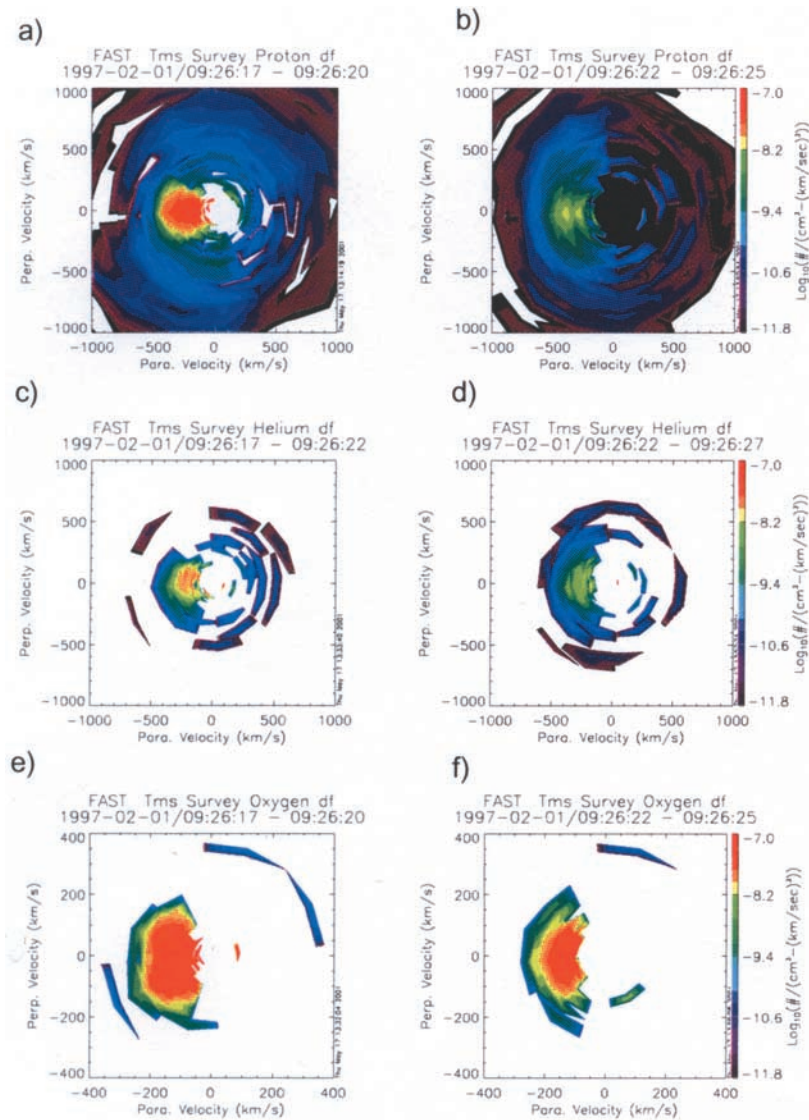
Figure 10. Ion heating: (a, b) proton distributions in the ion beam region of Figure 1 for when harmonic wave activity is absent and present, respectively; (c, d) the distributions for He$^+$ ions measured at the same times as Figures 10a and 10b; and (e, f) the same for O$^+$ ions.

Landau resonant with the ion beam. However, since the wave here occurs at frequencies very close to Ω_p, the beam's ions are also cyclotron resonant with the wave and in fact contribute the wave growth as discussed in section 3. This interaction is very similar to the Doppler-shifted cyclotron resonance studied by *Chaston et al.* [2000] in the plasma sheet boundary layer where a quasi-linear study showed strong diffusion in the perpendicular direction as observed here. For the coherent case, Figures 11a and 11b show the result from a test particle simulation using the calculated wave dispersion for ions of various energies streaming up the field line from 3000 km under the influence of their magnetic moment and a parallel electric field of 2 mV/m^{-1}. At 3700 km they enter the source region of the cyclotron waves, where we have assumed a monochromatic wave with $k_\perp \rho_{it} = 1$ ($\lambda = 1100$ m) at 200 Hz. This frequency naturally provides the cutoff at 3700 km since the minimum frequency from the dispersion results is $\omega/\Omega p = 0.9$. The protons with the slowest initial speeds remain in strong

resonance with the wave for the longest time and therefore experience the greatest energy gain due to interaction with the waves. The more energetic protons after entering the region where wave power exists pass through the altitude where they are resonant more quickly, and as their phase fluctuates from in-phase to antiphase with the wave field, their energy oscillates. The resulting energy gain is nearly all in the perpendicular direction except for the small contribution made from $\mathbf{v} \times \mathbf{B_1}$. We have plotted this energy change as Δv^2 to allow easy plotting of all three ion beam species. If the mechanism suggested by *Miura et al.* [1983] is in operation, we should expect to see in the data significant heating of He$^+$ and O$^+$ in addition to H$^+$ and particularly in the parallel direction. However, the He$^+$ and O$^+$ beam ions shown in Figures 10c–10f instead show considerably smaller changes in the angular width or perpendicular temperature particularly for the O$^+$ beam ions. The increased angular width of the He$^+$ ion beam is perhaps due to gyroresonant interaction with the ion waves
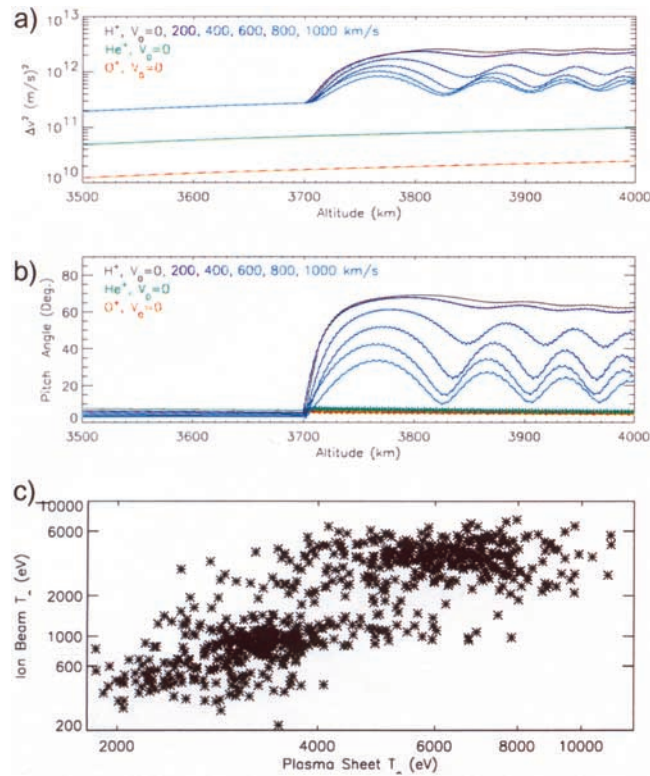
Figure 11. Simulation results: (a,b) the change in velocity squared (Δv^2) and pitch angle for hydrogen, helium, and oxygen ions streaming upward along field lines with varying initial parallel velocities and interacting with waves obeying the dispersion of the ion cyclotron fundamental with a cutoff at 3700 km altitude, and (c) the observed dependence of the perpendicular ion beam temperature on ion plasma sheet temperature. Plasma sheet temperatures have been obtained from the perpendicular second-order moment of the downgoing ion distribution that is dominated by plasma sheet ions, while the perpendicular ion beam temperature follows from the perpendicular second-order moment of the upgoing ion distribution that is dominated by beam ions.

below Ω_p shown in Figure 1, which occur at the same time as the harmonic waves but are not included in the simulation.

[42] The energy gain for the protons is limited by finite gyroradius effects. The most slowly moving protons, indicated by the black trace, gain an energy of 8870 eV or approximately $1/2 m_e v_{\perp it}$ as used in the modeling. Wave heating effectively ceases when the gyroradius approaches the perpendicular wavelength since the particles can no longer remain in resonance with the wave. Since the instability is centered at $k_\perp \rho_{it} = 1$, the temperature of the heated ions should follow that of the plasma sheet. This dependence can clearly be seen in Figure 11c, which shows how the observed perpendicular temperature of the ion beam increases with increasing plasma sheet temperature throughout the case study.

6.3. Beam Speeds and Wave Properties

[43] It has been shown that $v_{oeb}/v_{eb} > 1$ may persist without exciting violent broadband growth through the strong damping provided by the plasma sheet electrons when distributed as a shell. In fact, the threshold current for instability in the regime studied here requires $v_{oeb}/v_{eb} > 2.3$ for the electron beam component. Based purely on a moment analysis for the whole plasma, this drift is approximately twice the threshold for current-driven instability as

calculated by *Kindel and Kennel* [1971], who consider a two-component ion and electron plasma. In this way the electrons when distributed as a shell can carry appreciably more current before becoming unstable. In fact, as shown in Figure 8b when the distributions are instead modeled as Maxwellians, we find violent broadband growth that could be expected to produce large anomalous resistivity and significantly disrupt the beam. Instead, in this case the large, coherent parallel electric field component of the wave modulates the electron fluxes as shown in Figure 1b. Given that $k_\perp/k_\parallel$ as modeled is $\sim$7.7 and the observations of plasma sheet temperature and interferometry suggest a perpendicular wavelength of 1000 m with a perpendicular wave field of 500 mV/m^{-1} then the net potential drop in the parallel wave field is of the order of 1 keV over half a cycle. This is consistent with a shift in the mono-energetic peak for the observed distributions and as reported previously from observations by *McFadden et al.* [1998a]. This indicates that these waves significantly affect the current-carrying electrons that generate them and do so in a coherent manner. The contribution of these waves, which may reach amplitudes of 1 V/m^{-1}, to the resistivity of the plasma may be a significant factor for inclusion in current voltage studies in the auroral oval.

[44] The nonlinearity of the waveforms at Ω_p is most likely the source of the observed harmonic structure. There

are several features of the observed spectra that suggest this to be the case. Firstly, the regularity in the spacing and spectral energy of each harmonic makes the interpretation of each as an independent wave mode unlikely. The spacing is almost exactly multiples of the fundamental in both the electric and magnetic field measurement (as discussed in section 2.2), and secondly each successive spectral peak is at a lower spectral energy density following a nearly exact progression. For example, the harmonics present in the magnetic spectrum shown in Figure 2 very closely follow a power law as a function of the harmonic number n, such that $P(n)/P(0) = (n + 1)^{-3.5}$, where $P(0)$ is the wave power at the fundamental. Also, from a theoretical point of view the operation of each harmonic as a separately operating instability seems unlikely. The model used here can only account for small wave growth at up to the second harmonic; however, we observe spectral peaks up to the sixth harmonic. To stimulate growth at higher harmonics requires larger drift speeds, which would excite rapid broadband growth at $k_\perp \rho_{it} < 1$. Such waves are not observed. We are, however, by no means claiming that all observations of waves at proton harmonics are due to nonlinearity of waveforms at the fundamental. Good examples of emissions stimulated by wave growth at proton harmonics in the aurora can be found in the work of *Andre et al.* [1986].

[45] The observed magnetic component of the waves (in fact, at times the waves become Alfvenic in this respect) is symptomatic of the low electron beam temperature and high beam drift energies, i.e., $v_{oeb}/v_{eb} > 1$. As has been shown in section 4, narrowband wave growth in this regime is only possible when the plasma sheet electrons occur as a shell (as is observed) rather than as a more monotonically varying function of particle energy, such as a Maxwellian. Such a configuration allows the Landau resonance to occur at smaller $k_\parallel$, where as indicated by Figure 6d, the waves become significantly more electromagnetic, without exciting a more rapidly growing broadband electrostatic wave. Furthermore, the high beam speeds allow for coupling with the beam-plasma mode at parallel wave numbers where Landau resonant wave growth is occurring. This significantly enhances growth rates at these parallel wave numbers and lowers E_1/B_1 by an order of magnitude at $k_\perp \rho_{it} = 1$ (where maximum growth occurs). The effect of shifting the position of resonance to smaller $k_\parallel$ is clearly demonstrated both theoretically and from the data in Figure 8b, where the wave is shown to become more magnetic with increasing beam energy. There are also other parameters (though of lesser importance) that alter E_1/B_1, and these may contribute to the large scatter in E_1/B_1 shown here. For example, the data (and modeling) indicate that electromagnetic character of the wave is also weakly dependent on the plasma sheet temperature. Significant increases in plasma sheet temperature correspond to increases in the amplitude of the magnetic component since the wave then occurs at smaller $k_\perp$, where E_1/B_1 on the electrostatic ion cyclotron surfaces is smaller.

6.4. Limitations

[46] Despite significant agreement between the modeling and observations, the model as presented here has significant limitations. Apart from the usual problems with infinite homogeneous linear theory, the modeling of the shell is somewhat limited since the temperature of the plasma sheet electrons (width of the shells' annulus) is linked to the width of the shell (temperature of the reduced electron distribution). This fixes the relationship between plasma sheet temperature and the magnitude of the potential drop in a nonphysical way. This is particularly true for higher electron beam energies or larger potential drops. From Figure 3 this can be seen as the "thickness" of the shell annulus (that looks like a horseshoe), which is significantly larger in the model (Figure 3d) than is observed (Figure 3b). This effectively reduces the ability of the shell to damp waves that grow with phase speeds less than electron velocity of the potential drop or beam velocity such as the intermediate beam-plasma mode. Consequently, a model that more accurately describes the width of the shell can be expected to provide larger growth rates at Ω_p without exciting the intermediate beam-plasma for larger values of v_{oeb}/v_{eb}. A more physically correct approach is to specify the distribution function in terms of velocity and pitch angle [*Lotko and Maggs*, 1981]. This was not attempted here since it significantly complicates the integral over the cyclotron resonance condition.

[47] Throughout, it has been assumed that the plasma is uniform over many ion gyroradii. Observations show, however, that the ion and electron beam energies may vary by keV over distances less than 1 km (approximately the plasma sheet ion gyroradius) [*McFadden et al.*, 1998b]. In this regard, *Gavrishchaka et al.* [2002] have shown how discrete electrostatic harmonics can be generated from gradients in the parallel drift speed of the ion beam when dv_{oib}/dx becomes a significant fraction of the ion gyrofrequency, where x is the distance traveled transverse to B_o. Simulations performed by these authors produce electric field time series and spectra remarkably similar to observations for $(dv_{oib}/dx)/\Omega_p$ approaching 1. The data indicate that there are indeed times when $(dv_{oib}/dx)/\Omega_p$ exceeds 0.1; however, there are also many instances when this value is very much less than 0.1 and the harmonic waves are still observed. Whether we are observing these waves after the ion beam gradient has been relaxed is unknown. However, given that the electron beam at these times is still able to excite the instability at Ω_p and that there is a 1:1 association between the appearance of these waves and a cold field-aligned electron beam component suggest that the primary source of free energy is the electron beam.

6.5. Broadband ELF

[48] An obvious application of the intermediate beam-plasma mode is to observations of broadband ELF (BBELF) [*Bonnell*, 1996; *Andre et al.*, 1998; *Ergun et al.*, 1998a, 1998b; *Wahlund et al.*, 1998]. *Singh et al.* [1985] suggested the possibility of the beam-plasma mode as an explanation for this wave phenomena for parameters perhaps not appropriate for the auroral regions. The intermediate beam-plasma mode for parameters seen within the auroral acceleration region, however, has spectral characteristics similar to observations. This is particularly true in regions of downward current where ionospheric electrons are accelerated to energies exceeding a keV upward along magnetic field lines [*Carlson et al.*, 1998] and the strongest BBELF emissions are observed [*Ergun et al.*, 1998a, 1998b]. The electron distributions in these regions are composed of a plasma sheet and accelerated ionospheric electrons most commonly

showing evidence for strong parallel heating, leading to a cigar-like shape in velocity space. For such conditions the intermediate beam-plasma mode becomes unstable even for drift speeds less than the parallel electron thermal speed since it is not subject to the strong damping provided by the electron shell found in the upward current region. Because of the large growth rates that result, the electron distribution is heated very rapidly in the parallel direction so that most of the time "plateaued" or "flattop" electron distributions are observed. Preliminary work using the observed electron and ion distributions for less intense events (where a positive slope in $f_e(v_\parallel)$ is observed) indicates that much of the observed wave spectra, including the occurrence of cyclotron harmonics for low beam energies, can be explained through the growth of this mode on the electron beam.

7. Conclusions

[49] In this report we have been able to show how an electromagnetic ion cyclotron wave may grow at Ω_p through inverse Landau resonance with a cool field-aligned electron beam with a beam speed greater than its thermal speed. This wave is the neutralized Bernstein mode. Violent broadband growth of the intermediate beam-plasma mode is retarded owing to strong damping provided by the adiabatically reflected plasma sheet electrons in the potential drop. The growing wave occurs with both forward and backward group velocities along the field line from the source of instability, and for some wave numbers the group speed goes to zero. This provides very large convective growth rates and allows the wave to remain indefinitely in resonance with the electron beam at a given altitude. This instability then accounts for the large-amplitude coherent waves that have spectra nearly always centered on $n\Omega_p$ over a range of altitudes. In addition, it accounts for observations of both upward and downward directed Poynting fluxes.

[50] Furthermore, we have shown the following:

1. For observed beam energies the electromagnetic wave at the fundamental may have E_1/B_1 values as low as c, consistent with observations.

2. The presence of percentages of cold plasma exceeding 5% of the total number density seems unlikely in regions where these waves are observed.

3. The ion beam also contributes to the wave growth of the electromagnetic wave through a Doppler-shifted ion proton cyclotron resonance and in the process experiences strong heating up to the ion plasma sheet temperature consistent with observations.

4. The ion plasma sheet loss cone drives an electrostatic instability for pure ion Bernstein waves also at $n\Omega_p$.

5. The intermediate beam-plasma mode for observed ion and electron distributions may account for broadband electrostatic waves in both the upward and downward current regions.

Appendix A

[51] The dispersion results presented in this report are determined in the usual way from the solution of the equation

$$Det[D] = 0, \qquad (A1)$$

using Newton's method, where D is the dispersion tensor. The components of this tensor are defined as

$$D_{xx} = \omega^2 - k_\parallel^2 c^2 + k^2 c^2 \sum_j S_{xxj}, \qquad (A2a)$$

$$D_{xy} = k^2 c^2 \sum_j S_{xyj}, \qquad (A2b)$$

$$D_{xz} = k_\perp k_\parallel c^2 + k^2 c^2 \sum_j S_{xzj}, \qquad (A2c)$$

$$D_{yx} = k^2 c^2 \sum_j S_{yxj}, \qquad (A2d)$$

$$D_{yy} = \omega^2 - k^2 c^2 + k^2 c^2 \sum_j S_{yyj}, \qquad (A2e)$$

$$D_{yz} = k^2 c^2 \sum_j S_{yzj}, \qquad (A2f)$$

$$D_{zx} = k_\parallel k_\perp c^2 + k^2 c^2 \sum_j S_{zxj}, \qquad (A2g)$$

$$D_{zy} = k^2 c^2 \sum_j S_{zyj}, \qquad (A2h)$$

$$D_{zz} = \omega^2 - k_\perp^2 c^2 + k^2 c^2 \sum_j S_{zzj}, \qquad (A2i)$$

where k^2 is $k_\parallel^2 + k_\perp^2$ and the tensor S is dependent the functional form of each component, j, in the plasma. The components of S for drifting bi-Maxwellians as presented in (3) is well documented [e.g., *Ronnmark*, 1982; *Davidson*, 1983; *Gary*, 1992], and for the trapped distribution of (2) the elements equivalent to those used here can be found in the work of *Ronnmark* [1982]. For the shell distribution as given by the first term in (1) the elements of S are as follows:

$$
\begin{aligned}
S_{xxs} = {} & \frac{\omega_s^2}{k^2 c^2} \frac{\Omega_s^2}{k_\perp^2} \frac{n_s}{k_\parallel v_s} \frac{2 e^{-\lambda_s}}{(C^2 + 3 v_s^2)} \\
& \cdot \sum_{-\infty}^{\infty} n^2 \left\{ Z(\zeta_s) \left[\lambda_s \left(-I_n + I_n' \right) + \zeta_s^2 I_n + \frac{C^2}{v_s^2} I_n \right] + \zeta_s I_n \right\},
\end{aligned}
$$
$$(A3a)$$

$$
\begin{aligned}
S_{xys} = {} & \frac{i \omega_s^2}{k^2 c^2} \frac{n_s v_s}{(C^2 + 3 v_s^2)} \frac{e^{-\lambda_s}}{k_\parallel} \\
& \cdot \sum_{-\infty}^{\infty} n \left\{ Z(\zeta_s) \left[-I_n + I_n'/2 + \frac{3 \lambda_s I_n}{2} - 2 \lambda_s I_n' + \frac{n^2}{2 \lambda_s} I_n' \right] \right. \\
& \left. + \lambda_s I/2 - \left(\frac{C^2}{v_s^2} + \zeta_j^2 \right) \left(I_n'' - I_n \right) \right] - \zeta_s \left(I_n' - I_n \right) \right\},
\end{aligned}
$$
$$(A3b)$$

$$
\begin{aligned}
S_{xzs} = {} & \frac{\omega_s^2}{k^2 c^2} \frac{n_s}{(C^2 + 3 v_s^2)} \frac{\Omega_s}{k_\perp} \frac{e^{-\lambda_s}}{k_\parallel} \\
& \cdot \sum_{-\infty}^{\infty} n \left[Z'(\zeta_s) \left(\lambda_s I_n - \lambda_s I_n' - \zeta_s^2 I_n - \frac{C^2}{v_s^2} I_n \right) \right],
\end{aligned}
$$
$$(A3c)$$

$$S_{yxs} = -S_{xys}, \qquad (A3d)$$

$$S_{yys} = \frac{\omega_s^2}{k^2 c^2} \frac{n_s v_s}{(C^2 + 3v_s^2)} \frac{e^{-\lambda_s}}{k_\parallel} \sum_{-\infty}^{\infty} \left(\left(Z(\zeta_s) \left\{ \frac{\lambda_s}{2} [(1-\lambda_s)I_n \right. \right. \right.$$
$$+ (3\lambda_s - 2)I_n' + (2-\lambda_s)I_n'' + I_n'''] + \left(1 + \frac{C^2}{v_s^2}\right)$$
$$\cdot \left(\frac{n^2}{\lambda_s} I_n + 2\lambda_s I_n - 2\lambda_s I_n' \right) \right\}$$
$$\left. \left. - \frac{\zeta_s}{2} Z'(\zeta_s) \left(\frac{n^2}{\lambda_s} I_n + 2\lambda_s I - 2\lambda_s I_n' \right) \right) \right), \tag{A3e}$$

$$S_{yzs} = \frac{i\omega_s^2}{k^2 c^2} \frac{n_s}{(C^2 + 3v_s^2)} \frac{k_\perp}{\Omega_s} \frac{v_s^2}{2k_\parallel} \frac{e^{-\lambda_s}}{}$$

$$\cdot \sum_{-\infty}^{\infty} \left\{ Z'(\zeta_s) \left[-(I_n - I_n') \left(\frac{1}{2} + \zeta_s + \frac{C^2}{v_s^2} \right) \right. \right.$$
$$\left. \left. -I_n + 3\lambda_s I_n - 4\lambda_s I_n' + \frac{n^2}{\lambda_s} I_n + \lambda I_n'' \right] \right\}, \tag{A3f}$$

$$S_{zxs} = S_{xzs}, \tag{A3g}$$

$$S_{zys} = -S_{yzs}, \tag{A3h}$$

$$S_{zzs} = \frac{\omega_s^2}{k^2 c^2} \frac{n_s}{(C^2 + 3v_s^2)} \frac{v_s}{k_\parallel} \frac{e^{\lambda_s}}{}$$

$$\cdot \sum_{-\infty}^{\infty} \zeta_s \left[Z'(\zeta_s) \left(\lambda_s I_n - \lambda_s I_n' - \zeta_s^2 I_n - \frac{C^2}{v_s^2} I_n \right) + I_n \right], \tag{A3i}$$

where ω_j is the plasma frequency, ζ_s is $(\omega - n\Omega_s)/k_\parallel v_s$, λ_s is $(k_\perp v_{\perp s}/\Omega_s)^2$, Z is the plasma dispersion function determined numerically using the Pade approximation [*Ronnmark*, 1982], and I_n is the modified Bessel function of nth order.

References

Andre, M., Ion waves generated by streaming particles, *Ann. Geophys.*, *3*, 73, 1985a.

Andre, M., Dispersion surfaces, *J. Plasma. Phys.*, *33*, 1, 1985b.

Andre, M., M. Temerin, and D. Gorney, Resonant generation of ion waves on auroral field lines by positive slopes in ion velocity space, *J. Geophys. Res.*, *91*, 3145, 1986.

Andre, M., P. Norqvist, L. Andersson, L. Eliasson, A. I. Eriksson, L. Blomberg, R. E. Erlandson, and J. Waldemark, Ion ingratiation mechanisms at 1700 km in the auroral region, *J. Geophys. Res.*, *103*, 4199, 1998.

Bergmann, R., Electrostatic ion (hydrogen) cyclotron and ion acoustic wave instabilities in regions of upward field-aligned current and upward ion beams, *J. Geophys. Res.*, *89*, 953, 1984.

Bonnell, J. W., P. Kintner, J.-E. Wahlund, K. Lynch, and R. Arnoldy, Interferometric determination of broadband ELF wave phase velocity within a region of transverse auroral ion acceleration, *Geophys. Res. Lett.*, *23*, 3297, 1996.

Carlson, C. W., et al., FAST observations in the downward current region: Energetic upgoing electron beams, parallel potential drops and ion heating, *Geophys. Res. Lett.*, *25*, 2017, 1998.

Cattell, C. A., F. S. Mozer, I. Roth, R. R. Anderson, R. C. Elphic, W. Lennartsson, and E. Ungstrup, ISEE 1 observations of electrostatic ion cyclotron waves in association with ion beams on auroral field lines from ~2.5 to 4.5 Re, *J. Geophys. Res.*, *96*, 11,421, 1991.

Cattell, C. A., et al., The association of electrostatic ion cyclotron waves, ion and electron beams and field-aligned currents: FAST observations of an auroral zone crossing near midnight, *Geophys. Res. Lett.*, *25*, 2053, 1998.

Chaston, C. C., et al., Characteristics of electromagnetic proton cyclotron waves along auroral field lines observed by FAST in regions of upward current, *Geophys. Res. Lett.*, *25*, 2057, 1998.

Chaston, C. C., Y. D. Hu, and B. J. Fraser, Quasi-linear ion cyclotron heating in the near-Earth magnetotail, *J. Geophys. Res.*, *105*, 5507, 2000.

Chiu, Y. T., and M. Schulz, Self-consistent particle and parallel electrostatic field distributions in the magnetospheric-ionospheric auroral region, *J. Geophys. Res.*, *83*, 629, 1978.

Davidson, R. C., Kinetic waves and instabilities in a uniform plasma, in *Handbook of Plasma Physics-Basic Plasma Physics 1*, edited by M. N. Rosenbluth et al., pp. 521–527, North-Holland, New York, 1983.

Delory, G. T., et al., FAST observations of electron distributions within AKR source regions, *Geophys. Res. Lett.*, *25*, 2069, 1998.

Elphic, R. C., et al., The auroral current circuit and field-aligned currents observed by FAST, *Geophys. Res. Lett.*, *25*, 2033, 1998.

Ergun, R. E., et al., FAST satellite observations of electric field structures in the auroral zone, *Geophys. Res. Lett.*, *25*, 2025, 1998a.

Ergun, R. E., et al., FAST satellite observations of large-amplitude solitary structures, *Geophys. Res. Lett.*, *25*, 2041, 1998b.

Ergun, R. E., C. W. Carlson, J. P. McFadden, F. S. Mozer, and R. J. Strangeway, Parallel electric fields in discrete arcs, *Geophys. Res. Lett.*, *27*, 4053, 2000.

Erlandson, R. E., and L. J. Zanetti, A statistical study of auroral electromagnetic ion cyclotorn waves, *J. Geophys. Res.*, *103*, 4627, 1998.

Fredericks, R. W., Structure of generalized Bernstein modes from the full electromagnetic dispersion relation, *J. Plasma Phys.*, *2*, 381, 1968.

Fried, B. D. and S. D. Conte, *The Plasma Dispersion Function*, Academic, San Diego, Calif., 1961.

Gary, S. P., The mirror and ion cyclotron anisotropy instabilities, *J. Geophys. Res.*, *97*, 8519, 1992.

Gavrishchaka, V., G. Ganguli, W. Scales, S. Slinker, C. C. Chaston, J. P. McFadden, R. E. Ergun, and C. W. Carlson, Multi-scale coherent structures and broadband waves due to parallel inhomogeneous flows, *Phys. Rev. Lett.*, in press, 2002.

Glassmeier, K. H., A. J. Coates, M. H. Acuna, M. L. Goldstein, A. D. Johnstone, F. M. Neubauer, and H. Reme, Spectral characteristics of low frequency plasma turbulence upstream of comet P/Halley, *J. Geophys. Res*, *94*, 37, 1989.

Kauffman, R. L., and P. M. Kintner, Upgoing ion beams, 1, Microscopic analysis, *J. Geophys. Res.*, *87*, 10487, 1982.

Kauffmann, R. L., and P. M. Kintner, Upgoing ion beams, 2, Fluid analysis and magnetosphere ionosphere coupling, *J. Geophys. Res.*, *89*, 2195, 1984.

Kindel, J. M., and C. F. Kennel, Topside current instabilities, *J. Geophys. Res.*, *76*, 3055, 1971.

Kintner, P. M., M. C. Kelley, R. D. Sharp, A. G. Ghielmetti, M. Temerin, C. Cattell, P. F. Mizera, and J. F. Fennell, Simultaneous observations of energetic (keV) upstreaming and electrostatic hydrogen cyclotron waves, *J. Geophys. Res.*, *84*, 7201, 1979.

Koskinen, Observations of magnetospheric waves and their relation to precipitation, *Space Sci. Rev.*, *80*, 133, 1997.

Lotko, W., Diffusive acceleration of auroral primaries, *J. Geophys. Res.*, *91*, 191, 1986.

Lotko, W., and J. E. Maggs, Amplification of electrostatic noise in cyclotron resonance with an adiabatic auroral beam, *J. Geophys. Res.*, *86*, 3449, 1981.

Lund, E. J., et al., FAST observations of preferentially accelerated He$^+$ in associated with auroral electromagnetic ion cyclotron waves, *Geophys. Res. Lett.*, *25*, 2049, 1998.

McFadden, J. P., et al., Electron modulation and ion cyclotron waves observed by FAST, *Geophys. Res. Lett.*, *25*, 2045, 1998a.

McFadden, J. P., et al., Spatial structure and gradients of ion beams observed by FAST, *Geophys. Res. Lett.*, *25*, 2021, 1998b.

McFadden, J. P., R. E. Ergun, and C. W. Carlson, Ion and electron characteristics in auroral density cavities associated with ion beams: No evidence for cold ionospheric plasma, *J. Geophys. Res.*, *104*, 14,671, 1999.

Miura, A., H. Okuda, and M. Ashour-Abdalla, Ion-beam-driven electrostatic ion cyclotron instabilities, *Geophys. Res. Lett.*, *10*, 353, 1983.

Mozer, F. S., et al., Observations of paired electrostatic shocks in the polar magnetosphere, *Phys. Rev. Lett.*, *38*, 292, 1977.

Okuda, H., and K.-I. Nishikawa, Ion-beam-driven electrostatic hydrogen cyclotron waves on auroral fieldlines, *J. Geophys. Res*, *89*, 1023, 1984.

Oscarsson, T., A. Vaivads, K. Ronnmarck, J. H. Clemmons, H. de Feraudy, and B. Holback, Toward a self-consistent picture of the generation of electromagnetic ion cyclotron ELF waves on auroral field lines, *J. Geophys. Res.*, *102*, 24,369, 1997.

Perraut, S., et al., A systematic study of ULF waves above F_{H_+} from Geos and two measurements and their relationships with proton ring distributions, *J. Geophys. Res.*, *87*, 6219, 1982.

Pritchett, P. L., R. J. Strangeway, R. E. Ergun, J. P. McFadden, C. W. Carlson, and G. T. Delory, Free energy sources and frequency bandwidth for the auroral kilometric radiation, *J. Geophys. Res.*, *104*, 10,317, 1999.

Ronnmark, K., WHAMP-waves in a homogeneous, anisotropic, multi-component plasmas, *Rep. 179, Kiruna Geophys. Inst.*, Sweden, 1982.

Singh, N., J. R. Conrad, and R. W. Schunk, Electrostatic ion cyclotron, beam-plasma and lower hybrid waves excited by an electron beam, *J. Geophys. Res.*, *90*, 5159, 1985.

Smith, C. W., M. L. Goldstein, S. P. Gary, and C. T. Russell, Beam-driven ion cyclotron harmonic resonances in the terrestrial foreshock, *J. Geophys. Res.*, *90*, 1429, 1985.

Stenbaek-Nielsen, H. C., T. J. Hallinan, D. L. Osborne, J. Kimball, C. C. Chaston, J. McFadden, G. Delory, M. Temerin, and C. W. Carlson, Air-craft observations conjugate to FAST: Auroral arc thicknesses, *Geophys. Res. Lett.*, *25*, 2073, 1998.

Strangeway, R. J., et al., FAST observations of VLF waves in the auroral zone: Evidence of very low plasma densities, *Geophys. Res. Lett.*, *25*, 2065, 1998.

Temerin, M., and R. L. Lysak, Electromagnetic ion cyclotron (ELF) waves generated by auroral electron precipitation, *J. Geophys. Res.*, *89*, 2849, 1984.

Temerin, M., M. Woldorff, and F. S. Mozer, Nonlinear steepening of electrostatic ion cyclotron waves, *Phys. Rev. Lett.*, *43*, 1941, 1979.

Wahlund, J.-E., et al., Broadband ELF plasma emissions during auroral energisation, 1, Slow ion acoustic waves, *J. Geophys. Res.*, *103*, 4343, 1998.

————————————

J. W. Bonnell, C. W. Carlson, C. C. Chaston, R. E. Ergun, and J. P. McFadden, Space Sciences Laboratory, University of California, Centennial Drive at Grizzly Peak Blvd., Berkeley, CA 94720, USA. (ccc@ssl.berkeley.edu)